Energy stable flux reconstruction schemes for advection–diffusion problems on triangles

D.M. Williams [a],*, P. Castonguay [a], P.E. Vincent [b], A. Jameson [a]

[a] Department of Aeronautics and Astronautics, Stanford University, Stanford, CA 94305, USA
[b] Department of Aeronautics, Imperial College London, South Kensington, London SW7 2AZ, UK

ABSTRACT

The Flux Reconstruction (FR) approach unifies several well-known high-order schemes for unstructured grids, including a collocation-based nodal discontinuous Galerkin (DG) method and all types of Spectral Difference (SD) methods, at least for linear problems. The FR approach also allows for the formulation of new families of schemes. Of particular interest are the energy stable FR schemes, also referred to as the Vincent–Castonguay–Jameson–Huynh (VCJH) schemes, which are an infinite family of high-order schemes parameterized by a single scalar. VCJH schemes are of practical importance because they provide a stable formulation on triangular elements which are often required for numerical simulations over complex geometries. In particular, VCJH schemes are provably stable for linear advection problems on triangles, and include the collocation-based nodal DG scheme on triangles as a special case. Furthermore, certain VCJH schemes have Courant–Friedrichs–Lewy (CFL) limits which are approximately twice those of the collocation-based nodal DG scheme. Thus far, these schemes have been analyzed primarily in the context of pure advection problems on triangles. For the first time, this paper constructs VCJH schemes for advection–diffusion problems on triangles, and proves the stability of these schemes for linear advection–diffusion problems for all orders of accuracy. In addition, this paper uses numerical experiments on triangular grids to verify the stability and accuracy of VCJH schemes for linear advection–diffusion problems and the nonlinear Navier–Stokes equations.

© 2013 Elsevier Inc. All rights reserved.

1. Introduction

High-order methods for unstructured grids have the potential to solve notoriously challenging flow problems, in particular those which require high levels of accuracy in complex domains. However, despite several decades of development, their use within both academia and industry remains limited. There are several reasons for this situation, including difficulties generating high-order curved element meshes, difficulties resolving discontinuous solutions such as shock waves, and the general complexity of such methods relative to more standard low-order schemes, which are currently used widely to solve real-world problems of practical interest.

Traditional high-order methods for unstructured grids, such as the discontinuous Galerkin (DG) schemes proposed in [1–3], are based on a 'method of weighted residuals' formulation. Hence their implementations usually require quadrature procedures to be implemented and employed. However, in recent years, various unstructured high-order schemes based directly on differential forms of the governing system have emerged, such as Spectral Difference (SD) methods [4,5] and,

---

more generally, Flux Reconstruction (FR) methods [6]. For convenience, such schemes will henceforth be referred to as 'FR type' schemes. FR type schemes do not require integration to be performed, and hence their implementations can (explicitly at least) omit quadratures. As such, efficient implementation of FR type schemes is straightforward relative to their more traditional counterparts. Consequently, it is envisaged that such FR type methods will become popular amongst a wide community of fluid dynamicists within both academia and industry.

In what follows, a review of FR type methods is provided in order to establish the context and motivation for the current work. First proposed by Huynh in 2007, FR is an approach which generates new high-order schemes and recovers well-known schemes, including a variety of collocation-based nodal DG and SD schemes [6]. In the FR approach, the flux is subject to a reconstruction procedure involving 'correction functions' which are required to be polynomials of one degree higher than the solution (as well as satisfying symmetry, and boundary constraints). The FR approach was originally formulated for advection problems in 1D and was extended (via tensor products) to quadrilateral elements in 2D [6]. In 2009, Huynh formulated an extension of the FR approach to diffusion problems [7] in which both the solution and the flux are subject to reconstruction procedures. In both [6] and [7], Fourier analysis was employed in an effort to evaluate the stability of various FR schemes for linear advection and diffusion problems. Thereafter, Huynh developed an extension of the FR approach to advection–diffusion problems on triangles [8]. This approach makes use of scalar-valued, 2D correction functions, which are required to satisfy symmetry conditions similar to those imposed on the 1D correction functions. To the authors' knowledge, Fourier analysis of these schemes has yet to be performed.

In 2009, Gao and Wang identified a closely related class of schemes for advection–diffusion problems, referred to as Lifting Collocation Penalty (LCP) schemes [9,10]. These schemes make use of 'weighting functions' which are different from correction functions in that they are piecewise continuous polynomials that are of one degree lower than the correction functions. The LCP approach involves multiplying the governing equations by the weighting functions and integrating the result in order to obtain 'corrections'. These corrections are similar in form to those that arise in Huynh's FR approach [6,7], and under certain circumstances in 1D, the two approaches can be shown to be identical [11]. As a result, Wang, Gao, Haga, and Yu have referred to the class of all FR and LCP schemes as 'Correction Procedure via Reconstruction' (CPR) schemes [11,12], although it is not yet clear whether all FR schemes are in fact LCP schemes or vice versa. Wang, Gao, and Haga have provided evidence for the stability of the schemes, successfully applying the FR and LCP schemes to nonlinear advection–diffusion problems on grids of quadrilaterals and triangles in 2D [9] and tetrahedra and prisms in 3D [12,13].

In addition to being related to the LCP schemes, the FR schemes are also related to the Summation By Parts Simultaneous Approximation Term (SBP-SAT) finite difference schemes. The SBP-SAT and FR formulations are similar in that the SBP-SAT formulation can recover the 2nd order Galerkin Finite Element scheme on triangles [14] which (for a linear solution basis) is akin to the collocation-based nodal DG approach that the FR formulation recovers. However, SBP-SAT schemes of the form given by [14] cannot recover Galerkin Finite Element methods for non-simplex elements [15], and (thus far) have not been extended to yield compact high-order discretizations on triangles. For this reason, the SBP-SAT schemes will not be discussed further, although the interested reader should consult [16–19] for details pertaining to these schemes. The remainder of this discussion will instead focus on FR type schemes which are more closely related to the schemes of Huynh [6–8], and Gao and Wang [9,10].

Recently, efforts have focused on rigorously proving the stability of FR type schemes using 'energy methods'. Such methods offer advantages over von Neumann techniques (i.e., Fourier analysis) since they automatically extend to all orders of accuracy, and are valid for unstructured grids. In 2010, Jameson [20] used an energy method to prove stability of a particular SD method for linear advection problems. Subsequently, in 2011, Vincent, Castonguay, and Jameson [21] used a similar approach to derive an entire class of stable FR schemes for linear advection problems in 1D. These stable schemes, referred to as Vincent–Castonguay–Jameson–Huynh (VCJH) schemes, are parameterized by a single scalar. The scalar influences the analytical form of the correction functions, and variations of the scalar lead to recovery of various known numerical methods, including a collocation-based nodal DG method, the SD method that Jameson [20] proved to be stable for linear advection, and Huynh's so-called $g2$ method [6]. Recently, Castonguay and Williams et al. [22,23] extended the VCJH schemes, and proved their stability for advection–diffusion problems in 1D [23,24].

In 2D, Castonguay, Vincent, and Jameson used an energy method to identify a class of VCJH schemes which they proved to be stable for linear advection problems on triangles [25]. These schemes make use of vector-valued, 2D correction functions, which are required to satisfy symmetry and orthogonality conditions. The VCJH schemes on triangles are parametrized by a single scalar (as in the 1D case) which, if set to the correct value, allows for recovery of the collocation-based nodal DG scheme [25].

Note that the symmetry conditions used to define the VCJH correction functions due to Castoguay et al. [25] are different than those used to define the correction functions due to Huynh [8], and thus it does not appear that these two classes of schemes are equivalent. In addition, because VCJH schemes due to Castonguay et al. [25] utilize correction functions and LCP schemes due to Gao and Wang [10] utilize weighting functions, the equivalence of the VCJH and LCP classes of schemes has yet to be demonstrated.

In summary, a number of authors have proposed FR type approaches for the treatment of advection and advection–diffusion problems in 1D and on triangles. However, for linear advection problems, only the VCJH approaches of [21] in 1D and [25] on triangles have been proven stable for all orders of accuracy. Furthermore, for linear *advection–diffusion* problems on triangles, the approach of [25] has not yet been proven stable. This article will extend the approach of [25], to provide for the first time on triangles, a provably stable family of FR schemes for linear advection–diffusion problems.

The format of the paper is as follows. Section two presents a FR approach for solving advection–diffusion problems on triangles. Section three introduces the VCJH correction fields on triangles. Section four develops a range of VCJH schemes for linear advection–diffusion problems on triangles, and proves that these schemes are stable. Section five presents results of linear numerical experiments for the newly proposed schemes. Finally, the sixth section presents numerical experiments examining the stability of the VCJH schemes for nonlinear problems, with the aim of assessing how well the VCJH schemes perform in a more practical setting.

2. Flux reconstruction approach for advection–diffusion problems on triangles

In what follows, the FR schemes for advection problems on triangles, developed by Castonguay et al. in [25], are extended to *advection–diffusion* problems. For readers unfamiliar with the FR approach, the authors recommend a review of the 1D descriptions of FR for advection in [6,21], or advection–diffusion in [23] before proceeding further.

2.1. Preliminaries

Consider the 2D conservation law

$$\frac{\partial u}{\partial t} + \nabla \cdot \mathbf{f}(u, \nabla u) = 0, \tag{1}$$

where u is a scalar variable and $\mathbf{f}$ is a vector-valued flux. Eq. (1) can be rewritten as a first-order system,

$$\frac{\partial u}{\partial t} + \nabla \cdot \mathbf{f}(u, \mathbf{q}) = 0, \tag{2}$$

$$\mathbf{q} - \nabla u = 0. \tag{3}$$

The solution $u = u(x, y, t)$ to the system evolves inside the 2D domain $\boldsymbol{\Omega}$ (with boundary $\boldsymbol{\Gamma}$), where x and y are spatial coordinates, $\mathbf{q} = (q_x, q_y)$ is the auxiliary variable with components $q_x = q_x(u, \nabla u)$ and $q_y = q_y(u, \nabla u)$, and $\mathbf{f} = (f, g)$ has components $f = f(u, \mathbf{q})$ and $g = g(u, \mathbf{q})$. Assume that the domain $\boldsymbol{\Omega}$ can be discretized into N non-overlapping, conforming, straight-sided triangular elements $\boldsymbol{\Omega}_n$ such that

$$\boldsymbol{\Omega} = \bigcup_{n=1}^{N} \boldsymbol{\Omega}_n. \tag{4}$$

Approximations to Eqs. (2) and (3) can be constructed within each element $\boldsymbol{\Omega}_n$. In Eq. (2), the exact solution u can be replaced by an approximate solution $u_n^D = u_n^D(x, y, t)$, which is a two-dimensional polynomial of degree p within $\boldsymbol{\Omega}_n$ and is identically zero outside the element. In general, the sum of u_n^D and u_{n+1}^D is discontinuous at the interface between neighboring elements $\boldsymbol{\Omega}_n$ and $\boldsymbol{\Omega}_{n+1}$, and as a result each quantity is designated with a superscript D.

The flux $\mathbf{f}$ in Eq. (2) can be approximated by a function $\mathbf{f}_n = (f_n, g_n) = \mathbf{f}_n(x, y, t)$, which is a polynomial of degree $p + 1$ within $\boldsymbol{\Omega}_n$ and is identically zero outside $\boldsymbol{\Omega}_n$. The normal components of $\mathbf{f}_n$ and $\mathbf{f}_{n+1}$ are required to be equivalent to one another on the boundary between $\boldsymbol{\Omega}_n$ *and* $\boldsymbol{\Omega}_{n+1}$.

Analogous approximations can be introduced into Eq. (3). Here, the auxiliary variable $\mathbf{q}$ can be replaced by a function $\mathbf{q}_n^D = (q_x^D, q_y^D)_n = \mathbf{q}_n^D(x, y, t)$ which is a polynomial of degree p within $\boldsymbol{\Omega}_n$ and is identically zero outside. In general, the sum of $\mathbf{q}_n^D$ and $\mathbf{q}_{n+1}^D$ is discontinuous at the interface between $\boldsymbol{\Omega}_n$ and $\boldsymbol{\Omega}_{n+1}$. In addition, the exact solution u can be replaced by an approximate solution $u_n = u_n(x, y, t)$, which is a polynomial of degree $p + 1$ within $\boldsymbol{\Omega}_n$ and is identically zero outside (and where it is important to note that $u_n \neq u_n^D$). The approximate solutions u_n and u_{n+1} are required to be equivalent to one another on the boundary between $\boldsymbol{\Omega}_n$ and $\boldsymbol{\Omega}_{n+1}$.

Based on these definitions, the approximate first-order system within each element $\boldsymbol{\Omega}_n$ becomes

$$\frac{\partial u_n^D}{\partial t} + \nabla \cdot \mathbf{f}_n = 0, \tag{5}$$

$$\mathbf{q}_n^D - \nabla u_n = 0. \tag{6}$$

Next, in order to facilitate implementation, each element $\boldsymbol{\Omega}_n$ in physical space is mapped to a reference right triangle $\boldsymbol{\Omega}_S$. The mapping $\boldsymbol{\Theta}_n$ for a linear triangular element is

$$\mathbf{x} = \boldsymbol{\Theta}_n(\mathbf{r}) = -\frac{(r+s)}{2}\mathbf{v}_{1,n} + \frac{(r+1)}{2}\mathbf{v}_{2,n} + \frac{(s+1)}{2}\mathbf{v}_{3,n}, \tag{7}$$

where $\mathbf{x} = (x, y)$ are the physical coordinates, $\mathbf{r} = (r, s)$ are the reference coordinates, $\mathbf{v}_{1,n}, \mathbf{v}_{2,n}$, and $\mathbf{v}_{3,n}$ are the vertex coordinates of the element $\boldsymbol{\Omega}_n$ in physical space, and $(-1, -1)$, $(1, -1)$, and $(-1, 1)$ are the vertex coordinates of the element $\boldsymbol{\Omega}_S$ in reference space. Once a mapping is established, the physical quantities $u_n, u_n^D, \mathbf{f}_n$, and $\mathbf{q}_n^D$ in the triangular element $\boldsymbol{\Omega}_n$ can be reformulated as transformed quantities $\hat{u}, \hat{u}^D, \hat{\mathbf{f}}$, and $\hat{\mathbf{q}}^D$ in the reference triangle $\boldsymbol{\Omega}_S$ using the following transformations due to Viviand [26] and Vinokur [27]

$$\hat{u} = J_n u_n(\boldsymbol{\Theta}_n(\mathbf{r}), t), \quad \hat{u}^D = J_n u_n^D(\boldsymbol{\Theta}_n(\mathbf{r}), t), \tag{8}$$

$$\hat{\mathbf{f}} = \begin{bmatrix} \hat{f} \\ \hat{g} \end{bmatrix} = J_n \mathbf{J}_n^{-1} \mathbf{f}_n, \quad \hat{\mathbf{q}}^D = \begin{bmatrix} \hat{q}_r^D \\ \hat{q}_s^D \end{bmatrix} = \hat{\nabla}\hat{u} = J_n \mathbf{J}_n^T \mathbf{q}_n^D, \tag{9}$$

where

$$\mathbf{f}_n = \begin{bmatrix} f_n \\ g_n \end{bmatrix}, \quad \mathbf{q}_n^D = \begin{bmatrix} q_{x_n}^D \\ q_{y_n}^D \end{bmatrix} = \nabla u_n, \tag{10}$$

and

$$\mathbf{J}_n = \begin{bmatrix} \frac{\partial x}{\partial r} & \frac{\partial x}{\partial s} \\ \frac{\partial y}{\partial r} & \frac{\partial y}{\partial s} \end{bmatrix}, \quad J_n = \det(\mathbf{J}_n). \tag{11}$$

In Eq. (9), the operator $\hat{\nabla}$ is defined as the gradient in the reference domain taken with respect to r and s (where thus far ∇ has been the gradient in the physical domain taken with respect to x and y).

The following identities arise from Eqs. (8)–(11)

$$\nabla \cdot \mathbf{f}_n = \frac{1}{J_n}\left(\hat{\nabla} \cdot \hat{\mathbf{f}}\right), \tag{12}$$

$$\nabla u_n \cdot \mathbf{f}_n = \frac{1}{J_n^2}\left(\hat{\nabla}\hat{u} \cdot \hat{\mathbf{f}}\right), \tag{13}$$

$$\int_{\boldsymbol{\Omega}_n} J_n u_n (\nabla \cdot \mathbf{f}_n) d\boldsymbol{\Omega}_n = \int_{\boldsymbol{\Omega}_S} \hat{u}\left(\hat{\nabla} \cdot \hat{\mathbf{f}}\right) d\boldsymbol{\Omega}_S, \tag{14}$$

$$\int_{\boldsymbol{\Omega}_n} J_n (\nabla u_n \cdot \mathbf{f}_n) d\boldsymbol{\Omega}_n = \int_{\boldsymbol{\Omega}_S} \hat{\nabla}\hat{u} \cdot \hat{\mathbf{f}} d\boldsymbol{\Omega}_S, \tag{15}$$

$$\int_{\boldsymbol{\Gamma}_n} J_n u_n (\mathbf{f}_n \cdot \mathbf{n}) d\boldsymbol{\Gamma}_n = \int_{\boldsymbol{\Gamma}_S} \hat{u}\left(\hat{\mathbf{f}} \cdot \hat{\mathbf{n}}\right) d\boldsymbol{\Gamma}_S. \tag{16}$$

These identities will be used extensively in the subsequent proof of the stability of VCJH schemes for the linear advection–diffusion problem on triangles (c.f. Section 4).

The governing equations (Eqs. (5) and (6)) in the physical domain can now be transformed to equivalent equations in the reference domain, using Eqs. (8)–(11). The result is

$$\frac{\partial \hat{u}^D}{\partial t} + \hat{\nabla} \cdot \hat{\mathbf{f}} = 0, \tag{17}$$

$$\hat{\mathbf{q}}^D - \hat{\nabla}\hat{u} = 0. \tag{18}$$

The next section will discuss the FR procedure for solving Eqs. (17) and (18).

2.2. Procedure

The FR approach for advection–diffusion problems on triangles consists of seven stages. In practice, when implementing the method, several of these stages can be combined, however, in what follows they will be presented as separate stages for the sake of clarity.

In the first stage of the FR approach on triangles, the approximate transformed solution $\hat{u}^D$ within the reference element $\boldsymbol{\Omega}_S$ is defined using a two-dimensional polynomial of degree p. The polynomial is constructed from values of the approximate transformed solution at $N_p = \frac{1}{2}(p+1)(p+2)$ solution points. (Fig. 1 shows an example of the locations of the solution points for the case of $p = 2$). The resulting approximate transformed solution takes the form

$$\hat{u}^D(\mathbf{r}, t) = \sum_{i=1}^{N_p} \hat{u}_i^D l_i(\mathbf{r}), \tag{19}$$

where $\hat{u}_i^D = J_n(\mathbf{r}_i) \cdot u_n^D(\boldsymbol{\Theta}_n(\mathbf{r}_i), t)$ is the value of $\hat{u}^D$ at solution point i, $\mathbf{r}_i$ is the location of solution point i, and $l_i(\mathbf{r})$ is the nodal basis function which takes on the value of 1 at solution point i and the value of 0 at all other solution points. The approximate transformed solution $\hat{u}^D$ lies in the space $P_p(\boldsymbol{\Omega}_S)$, where $P_p(\boldsymbol{\Omega}_S)$ defines the polynomial space of degree $\leqslant p$ on $\boldsymbol{\Omega}_S$. Consequently, $\hat{u}^D$ also lies in the polynomial space $R_p(\boldsymbol{\Gamma}_S) = \left\{ \phi | \phi \in L^2(\boldsymbol{\Gamma}_S), \phi|_{\boldsymbol{\Gamma}_f} \in P_p(\boldsymbol{\Gamma}_f), \forall \boldsymbol{\Gamma}_f \right\}$ which contains polynomials of degree $\leqslant p$ defined on each side $\boldsymbol{\Gamma}_f$ of $\boldsymbol{\Omega}_S$.

The second stage involves calculating common values for the transformed solution $\hat{u}^I$ at a set of flux points along the edges of $\boldsymbol{\Omega}_S$. In what follows, a quantity labeled with the indices f, j corresponds to a quantity at the flux point j of face f,
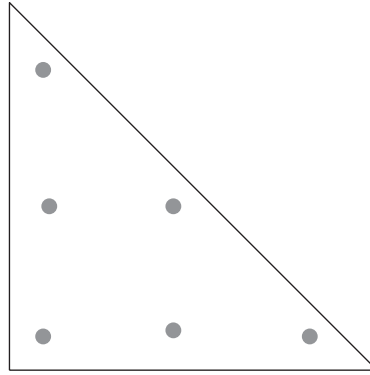
Fig. 1. Example of solution point locations (denoted by circles) in the reference element for $p = 2$.

where $1 \leqslant f \leqslant 3$ and $1 \leqslant j \leqslant N_{fp}$. Here, N_{fp} is the number of flux points on each face, and is equal to $p + 1$. The location of flux point j on face f is denoted $\mathbf{r}_{f,j}$. The convention used to number faces and flux points is illustrated in Fig. 2.

Common values of the transformed solution at each flux point ($\hat{u}^I_{f,j}$) are computed by first evaluating the multiply defined values of the physical solution $u^D_{f,j}$ at each flux point. At each flux point, $u^D_{(f,j)-}$ is defined as the value of $u^D_{f,j}$ computed using the information local to the current element and $u^D_{(f,j)+}$ as the value of $u^D_{f,j}$ computed using information from the adjoining element. For a given element, the physical solution at each flux point is obtained by evaluating the transformed solution ($\hat{u}^D$ in Eq. (19)) at each flux point, and converting the result to physical space using Eq. (8). Once both physical solution values ($u^D_{(f,j)-}$ and $u^D_{(f,j)+}$) are obtained, an approach such as the Central Flux (CF) [28], Local Discontinuous Galerkin (LDG) [29], Compact Discontinuous Galerkin (CDG) [30], Internal Penalty (IP) [31], Bassi Rebay 1 (BR1) [3], or Bassi Rebay 2 (BR2) approach [32] can be used to compute a common solution value $u^I_{f,j}$. The LDG approach is of particular interest because it is identical to the CDG approach in 1D, and recovers the BR1 and CF approaches in 1D, 2D, and 3D. If one elects to employ the LDG approach, the common solution value $u^I_{f,j}$ is computed as follows

$$u^I_{f,j} = \{\{u^D_{f,j}\}\} - \beta \cdot [\![u^D_{f,j}]\!], \quad \beta = (\beta_x, \beta_y), \tag{20}$$

where β is a directional parameter which allows $u^I_{f,j}$ to assume a value that is biased in either the upwind or downwind direction, and $\{\{\cdot\}\}$ and $[\![\cdot]\!]$ are 'average' and 'jump' operators, respectively which are defined such that

$$\{\{u^D_{f,j}\}\} = \frac{uD_{(f,j)-} + u^D_{(f,j)+}}{2}, \quad [\![u^D_{f,j}]\!] = u^D_{(f,j)-}\mathbf{n}_- + u^D_{(f,j)+}\mathbf{n}_+, \tag{21}$$

where $\mathbf{n}_-$ and $\mathbf{n}_+$ denote the outward and inward pointing unit normals, respectively.

Note that choosing $\beta = \pm 0.5\mathbf{n}_-$ promotes compactness of the FR scheme in multiple dimensions, but does not ensure it for certain cases on general grids [28,30]. Alternative approaches (such as CDG or BR2) can be employed to ensure compactness in multiple dimensions. These compact approaches are essential for cases in which the full matrix is to be formed, i.e., when
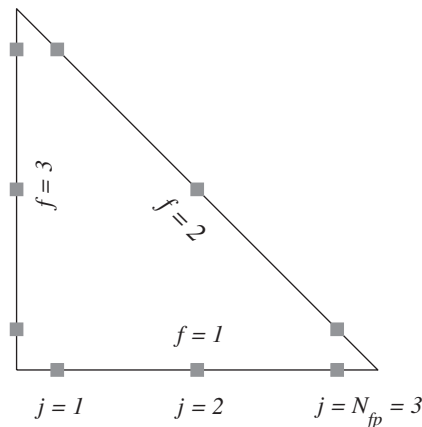

Fig. 2. Example of the numbering convention for the faces and flux points on the reference element for $p = 2$. The flux points are denoted by squares and the flux point index increases counter clockwise along an edge.

a spatial discretization is paired with an implicit time-stepping approach. However, this paper is concerned with demonstrating favorable aspects of pairing FR discretizations with *explicit* time-stepping approaches. In this context, compactness is less important, and the LDG approach is frequently sufficient.

After the common solution $u_{f,j}^l$ is computed using the LDG approach or an alternative approach, the transformed common solution denoted by $\hat{u}_{f,j}^l$ can be obtained from Eq. (8).

Next, in preparation for the third stage, one may compute $\hat{u}_{f,j}^C$ the transformed solution correction at each flux point as follows

$$\hat{u}_{f,j}^C = \hat{u}_{f,j}^l - \hat{u}_{f,j}^D. \tag{22}$$

Note that the superscript 'C' on $\hat{u}_{f,j}^C$ stands for 'correction.'

The third stage involves constructing the transformed auxiliary variable $\hat{\mathbf{q}}^D$ from the transformed solution correction $\hat{u}_{f,j}^C$ at each flux point. Towards this end, one may expand $\hat{\mathbf{q}}^D$ (in Eq. (18)) in order to obtain

$$\hat{\mathbf{q}}^D = \hat{\nabla}\hat{u} = \hat{\nabla}\hat{u}^D + \hat{\nabla}\hat{u}^C, \tag{23}$$

where $\hat{\nabla}\hat{u}^D$ is computed by applying the transformed gradient operator $\hat{\nabla}$ to $\hat{u}^D$ in Eq. (19), and $\hat{\nabla}\hat{u}^C$ is computed by 'lifting' values of $\hat{u}_{f,j}^C$ from the element boundary as follows

$$\hat{\nabla}\hat{u}^C(\mathbf{r}) = \sum_{f=1}^{3}\sum_{j=1}^{N_{fp}} \hat{u}_{f,j}^C \psi_{f,j}(\mathbf{r}) \hat{\mathbf{n}}_{f,j}. \tag{24}$$

The function $\psi_{f,j}$ is a 'correction field' or 'lifting operator' which transforms $\hat{u}^C$ defined on $\mathbf{\Gamma}_S$ into $\hat{\nabla}\hat{u}^C$ defined throughout $\mathbf{\Omega}_S$. Details regarding the construction of $\psi_{f,j}$ are given in Appendix A.

On rewriting Eq. (23) in terms of $\hat{u}^D$ from Eq. (19) and $\hat{\nabla}\hat{u}^C$ from Eq. (24), one obtains the following expression for $\hat{\mathbf{q}}^D$

$$\hat{\mathbf{q}}^D(\mathbf{r}) = \hat{\nabla}\hat{u}^D(\mathbf{r}) + \hat{\nabla}\hat{u}^C(\mathbf{r}) = \sum_{i=1}^{N_p} \hat{u}_i^D \hat{\nabla}l_i(\mathbf{r}) + \sum_{f=1}^{3}\sum_{j=1}^{N_{fp}} \hat{u}_{f,j}^C \psi_{f,j}(\mathbf{r}) \hat{\mathbf{n}}_{f,j}. \tag{25}$$

In the fourth stage, the transformed discontinuous flux $\hat{\mathbf{f}}^D$ can be computed using $\hat{u}^D$ from Eq. (19) and $\hat{\mathbf{q}}^D$ from Eq. (25). Each component of the flux $\hat{\mathbf{f}}^D = (\hat{f}^D, \hat{g}^D)$ can be expressed using a degree p polynomial as follows

$$\hat{f}^D(\mathbf{r}) = \sum_{i=1}^{N_p} \hat{f}_i^D l_i(\mathbf{r}), \quad \hat{g}^D(\mathbf{r}) = \sum_{i=1}^{N_p} \hat{g}_i^D l_i(\mathbf{r}), \tag{26}$$

where the quantities $\hat{f}_i^D$ and $\hat{g}_i^D$ are the components of the transformed flux at solution point i, and are evaluated using $\hat{u}_i^D$ and $\hat{\mathbf{q}}_i^D$.

The fifth stage involves calculating transformed numerical interface fluxes $\hat{\mathbf{f}}^l$ at flux points along the edges of $\mathbf{\Omega}_S$. At each flux point, the transformed flux $\hat{\mathbf{f}}_{f,j}^l$ is calculated based on the physical flux $\mathbf{f}_{f,j}^l$ which is composed from advective and diffusive parts $\mathbf{f}_{f,j}^l = \mathbf{f}_{(f,j)\,adv}^l + \mathbf{f}_{(f,j)\,dif}^l$. In turn, $\mathbf{f}_{(f,j)\,adv}^l$ and $\mathbf{f}_{(f,j)\,dif}^l$ are constructed from the multiply defined discontinuous fluxes at each flux point denoted by

$$\mathbf{f}_{(f,j)\,adv-}^D = \mathbf{f}\left(u_{(f,j)-}^D\right), \quad \mathbf{f}_{(f,j)\,adv+}^D = \mathbf{f}\left(u_{(f,j)+}^D\right), \tag{27}$$

$$\mathbf{f}_{(f,j)\,dif-}^D = \mathbf{f}\left(u_{(f,j)-}^D, \mathbf{q}_{(f,j)-}^D\right), \quad \mathbf{f}_{(f,j)\,dif+}^D = \mathbf{f}\left(u_{(f,j)+}^D, \mathbf{q}_{(f,j)+}^D\right). \tag{28}$$

The solution values $u_{(f,j)-}^D$ and $u_{(f,j)+}^D$ were obtained in stage 2, and the auxiliary variable values $\mathbf{q}_{(f,j)-}^D$ and $\mathbf{q}_{(f,j)+}^D$ are obtained by evaluating $\hat{\mathbf{q}}^D$ at each flux point using Eq. (25), and converting the result to physical space using Eq. (9).

Once $\mathbf{f}_{(f,j)adv-}^D$, $\mathbf{f}_{(f,j)adv+}^D$, $\mathbf{f}_{(f,j)dif-}^D$, and $\mathbf{f}_{(f,j)dif+}^D$ are obtained, the numerical advective flux $\mathbf{f}_{(f,j)adv}^l$ and the numerical diffusive flux $\mathbf{f}_{(f,j)dif}^l$ can be computed. For linear advection–diffusion equations, $\mathbf{f}_{(f,j)adv}^l$ can be computed using the Lax–Friedrichs approach (as defined in [28]), and for the nonlinear Navier–Stokes equations, $\mathbf{f}_{(f,j)adv}^l$ can be computed using a Roe [33] or Rusanov [34] approach. For both linear and nonlinear equations, the numerical diffusive flux $\mathbf{f}_{(f,j)dif}^l$ can be computed using one of the aforementioned CF, LDG, CDG, IP, BR1, or BR2 approaches. In particular, if one elects to employ the LDG approach, the common numerical diffusive flux is computed as follows

$$\mathbf{f}_{(f,j)\,dif}^l = \{\{\mathbf{f}_{(f,j)\,dif}^D\}\} + \tau[\![u_{f,j}^D]\!] + \beta[\![\mathbf{f}_{(f,j)\,dif}^D]\!], \tag{29}$$

where τ is a penalty parameter controlling the jump in the solution, β is the directional parameter (defined previously), and $\{\{\cdot\}\}$ and $[\![\cdot]\!]$ are the average and jump operators for the flux which are defined such that

$$\{\{\mathbf{f}_{(f,j)\,dif}^D\}\} = \frac{\mathbf{f}_{(f,j)\,dif-}^D + \mathbf{f}_{(f,j)\,dif+}^D}{2}, \tag{30}$$

$$[\![\mathbf{f}_{(f,j)\,dif}^D]\!] = \mathbf{f}_{(f,j)\,dif-}^D \cdot \mathbf{n}_- + \mathbf{f}_{(f,j)\,dif+}^D \cdot \mathbf{n}_+. \tag{31}$$

Note that the parameter β in Eq. (29) is preceded by a '+' sign and in Eq. (20) it is preceded by a '−' sign. Opposite signs help ensure symmetry of the diffusive process in the following sense: if the common solution $u_{f,j}^l$ is upwind biased then the numerical flux $\mathbf{f}_{(f,j)\,dif}^l$ is downwind biased or vice versa.

Once the total numerical flux $\mathbf{f}_{f,j}^l = \mathbf{f}_{(f,j)\,adv}^l + \mathbf{f}_{(f,j)\,dif}^l$ is computed, the transformed numerical flux denoted by $\hat{\mathbf{f}}_{f,j}^l$ can be obtained from Eq. (9).

The sixth stage involves forming the transformed flux correction $\hat{\mathbf{f}}^C$ which will be added to the transformed discontinuous flux $\hat{\mathbf{f}}^D$ to form the transformed continuous flux $\hat{\mathbf{f}}$ (i.e., $\hat{\mathbf{f}} = \hat{\mathbf{f}}^D + \hat{\mathbf{f}}^C$). $\hat{\mathbf{f}}^C$ is constructed using vector correction functions $\mathbf{h}_{f,j}(\mathbf{r})$ which are restricted to lie in the Raviart–Thomas space [35] of order p, denoted by $RT_p(\Omega_S)$. Note that $RT_p(\Omega_S) = (P_p(\Omega_S))^2 + \mathbf{r}P_p(\Omega_S)$, where $(P_p(\Omega_S))^2$ is the two-dimensional vector space with components with degree $\leqslant p$. As a consequence, the vector correction functions possess the following attributes

$$\phi_{f,j}(\mathbf{r}) \in P_p(\Omega_S), \quad \mathbf{h}_{f,j}(\mathbf{r}) \cdot \hat{\mathbf{n}}|_{\Gamma_S} \in R_p(\Gamma_S), \tag{32}$$

where

$$\phi_{f,j}(\mathbf{r}) \equiv \hat{\nabla} \cdot \mathbf{h}_{f,j}(\mathbf{r}) \tag{33}$$

is referred to as the 'correction field', and $\mathbf{h}_{f,j}(\mathbf{r}) \cdot \hat{\mathbf{n}}|_{\Gamma_S}$ is referred to as the 'normal trace'.

Furthermore, if k represents a particular face ($1 \leqslant k \leqslant 3$) and ℓ represents a particular flux point ($1 \leqslant \ell \leqslant N_{fp}$), each of the correction functions $\mathbf{h}_{f,j}$ is required to satisfy

$$\mathbf{h}_{f,j}(\mathbf{r}_{k,\ell}) \cdot \hat{\mathbf{n}}_{k,\ell} = \begin{cases} 1 & \text{if } f = k \text{ and } j = \ell \\ 0 & \text{if } f \neq k \text{ or } j \neq \ell. \end{cases} \tag{34}$$

Eqs. (32) and (34) ensure that the resulting FR schemes are conservative [25]. Fig. 3 shows an example of a vector correction function $\mathbf{h}_{f,j}$ which satisfies Eqs. (32) and (34) for the case of $p = 2$.

Now, having defined the vector correction functions $\mathbf{h}_{f,j}$, one may define the transformed flux correction $\hat{\mathbf{f}}^C$ as follows

$$\hat{\mathbf{f}}^C(\mathbf{r}) = \sum_{f=1}^{3} \sum_{j=1}^{N_{fp}} \left[\left(\hat{\mathbf{f}}_{f,j}^l - \hat{\mathbf{f}}_{f,j}^D \right) \cdot \hat{\mathbf{n}}_{f,j} \right] \mathbf{h}_{f,j}(\mathbf{r}) = \sum_{f=1}^{3} \sum_{j=1}^{N_{fp}} \Delta_{f,j} \mathbf{h}_{f,j}(\mathbf{r}). \tag{35}$$

Here, $\Delta_{f,j}$ is defined as the difference between the normal transformed numerical interface flux and the normal transformed discontinuous flux at the flux point f, j.

The final stage involves calculating the divergence of the continuous transformed flux $\hat{\mathbf{f}}$. The result is used to update the transformed solution at the solution point $\mathbf{r}_i$ as follows

$$\frac{d\hat{u}_i^D}{dt} = -\left(\hat{\nabla} \cdot \hat{\mathbf{f}}\right)\Big|_{\mathbf{r}_i} = -\left(\hat{\nabla} \cdot \hat{\mathbf{f}}^D\right)\Big|_{\mathbf{r}_i} - \left(\hat{\nabla} \cdot \hat{\mathbf{f}}^C\right)\Big|_{\mathbf{r}_i} = -\sum_{k=1}^{N_p} \left(\hat{f}_k^D\right) \frac{\partial l_k}{\partial r}\Big|_{\mathbf{r}_i} - \sum_{k=1}^{N_p} \left(\hat{g}_k^D\right) \frac{\partial l_k}{\partial s}\Big|_{\mathbf{r}_i} - \sum_{f=1}^{3} \sum_{j=1}^{N_{fp}} \Delta_{f,j} \phi_{f,j}(\mathbf{r}_i). \tag{36}$$

For triangles, the overall behavior of the FR scheme depends on six factors, namely:

1. The location of the solution points $\mathbf{r}_i$.
2. The location of the flux points $\mathbf{r}_{f,j}$.
3. The methodology for calculating the transformed common solution values $\hat{u}_{f,j}^l$.
4. The methodology for calculating the transformed numerical flux values $\hat{\mathbf{f}}_{f,j}^l$.
5. The form of the solution correction field $\psi_{f,j}$.
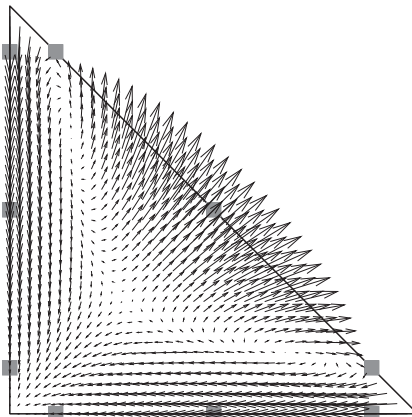6. The form of the flux correction field $\phi_{f,j}$.

Fig. 3. Example of a vector correction function $\mathbf{h}_{f,j}$ associated with flux point $f = 2, j = 2$ for $p = 2$.

The FR schemes can be simplified by choosing the same solution and flux correction fields (choosing $\psi_{f,j} = \phi_{f,j}$). Nevertheless, in an effort to generalize the subsequent discussions, the solution and flux correction fields are assumed to be distinct unless otherwise indicated.

Finally, note that the computational effort associated with the FR approach is identical to that associated with a collocation-based nodal DG approach. When the corrections fields are chosen appropriately, the FR approach recovers a collocation-based nodal DG scheme (as mentioned previously).

3. VCJH correction fields on triangles

For linear advection problems on triangles, Castonguay et al. [25] have identified a range of correction fields $\phi_{f,j}$ for correcting the flux, which lead to energy stable FR schemes. The correction fields $\phi_{f,j}$ are polynomials of degree p, and can therefore be expressed in terms of an orthonormal basis L_k of degree p as follows

$$\phi_{f,j} = \sum_{k=1}^{N_p} \sigma_k L_k(\mathbf{r}), \tag{37}$$

where the coefficients σ_k are constants. Here each L_k is a member of the 2D Dubiner basis [36] defined on the reference right triangle $\boldsymbol{\Omega}_S$. This basis is given by

$$L_k(\mathbf{r}) = \sqrt{2} Q_v(a) Q_w^{(2v+1,0)}(b)(1-b)^v, \tag{38}$$

$$k = w + (p+1)v + 1 - \frac{v}{2}(v-1), \quad (v,w) \geqslant 0, \quad v + w \leqslant p,$$

where

$$a = 2\frac{(1+r)}{(1-s)} - 1, \quad b = s, \tag{39}$$

and $Q_n^{(\alpha,\beta)}$ is the nth order Jacobi polynomial (normalized as described in [28]).

Castonguay et al. [25] showed that stability for linear advection problems can be achieved if the coefficients σ_k are computed by solving the following system of equations

$$\sum_{k=1}^{N_p} \sigma_k \sum_{m=1}^{p+1} c_m \left(D^{(m,p)} L_i \right) \left(D^{(m,p)} L_k \right) = -\sigma_i + \int_{\Gamma_S} (\mathbf{h}_{f,j} \cdot \hat{\mathbf{n}}) L_i \, d\Gamma_S \qquad \text{for } 1 \leqslant i \leqslant N_p, \tag{40}$$

where each dot product $(\mathbf{h}_{f,j} \cdot \hat{\mathbf{n}})$ is defined via Eq. (34), each derivative operator $D^{(m,p)}$ is of the form

$$D^{(m,p)} = \frac{\partial^p}{\partial r^{(p-m+1)} \partial s^{(m-1)}}, \quad 1 \leqslant m \leqslant p+1, \tag{41}$$

and each constant c_m is of the form

$$c_m = c \binom{p}{m-1} = c \left[\frac{p!}{(m-1)!(p-m+1)!} \right]. \tag{42}$$

In Eq. (42), c is a scalar, where $0 \leqslant c \leqslant \infty$. The correction fields $\phi_{f,j}$ obtained from the solution of Eq. (40) lead to VCJH schemes on triangles which are an infinite family of FR schemes parameterized by c. For linear advection problems on triangles, if $c = c_{dg} = 0$, a collocation-based nodal DG scheme is recovered [25].

The stability of VCJH schemes for linear advection problems on triangles (for which periodic boundary conditions can be imposed) is ensured because it can be shown that a Sobolev-type norm of the solution is non-increasing, i.e.,

$$\frac{d}{dt} \|U^D\|_{p,c}^2 \leqslant 0, \tag{43}$$

where the Sobolev-type norm is defined as

$$\|U^D\|_{p,c} = \left\{ \sum_{n=1}^{N} \int_{\boldsymbol{\Omega}_n} \left[(u_n^D)^2 + \frac{1}{A_S} \sum_{m=1}^{p+1} c_m \left(D^{(m,p)} u_n^D \right)^2 \right] d\boldsymbol{\Omega}_n \right\}^{1/2}, \tag{44}$$

U^D is the total (domain-wide) solution defined as

$$U^D = \sum_{n=1}^{N} u_n^D, \tag{45}$$

and A_S denotes the area of the reference element $\boldsymbol{\Omega}_S$. Note that, in Eq. (44), the derivative operator $D^{(m,p)}$ in $\boldsymbol{\Omega}_S$ has been applied to u_n^D in the physical domain $\boldsymbol{\Omega}_n$ using the chain rule.

4. Proof of stability of VCJH schemes for the linear advection–diffusion equation on triangles

In this section, it is shown that if the correction fields $\psi_{f,j}$ and $\phi_{f,j}$ are chosen to be VCJH correction fields, (i.e., $\psi_{f,j} = \hat{\nabla} \cdot \mathbf{g}_{f,j}$ and $\phi_{f,j} = \hat{\nabla} \cdot \mathbf{h}_{f,j}$ where $\mathbf{h}_{f,j}$ and $\mathbf{g}_{f,j}$ are VCJH vector correction functions), and the transformed common solution values $\hat{u}_{f,j}^I$ and numerical flux values $\hat{\mathbf{f}}_{f,j}^I$ are obtained appropriately, the resulting FR schemes are stable for the linear advection–diffusion equation on straight-sided triangles.

4.1. Preliminaries

The linear advection–diffusion equation in 2D can be expressed as the following first-order system

$$\frac{\partial u}{\partial t} + \nabla \cdot (\mathbf{a} u - b\mathbf{q}) = 0, \tag{46}$$

$$\mathbf{q} - \nabla u = 0, \tag{47}$$

where $\mathbf{a} = (a_x, a_y)$ is a velocity vector (with constant components) and b is a diffusivity coefficient (with constant value $b \geqslant 0$). Eqs. (46) and (47) can be rewritten in terms of physical coordinates in the nth element ($\boldsymbol{\Omega}_n$), yielding Eqs. (5) and (6), where $\mathbf{f}_n = \mathbf{f}_{adv,n} + \mathbf{f}_{dif,n}$, and where $\mathbf{f}_{adv,n} = \mathbf{a} u_n^D$ and $\mathbf{f}_{dif,n} = -b\mathbf{q}_n^D$.

4.2. The stability of VCJH schemes

The stability of VCJH schemes for linear advection–diffusion problems on triangles can be established by examining the evolution in time of the Sobolev-type norm of the solution given in Eq. (44). An expression for the time rate of change of this norm will be constructed using contributions from the solution itself u_n^D (Eq. (5)) and the auxiliary variable $\mathbf{q}_n^D$ (Eq. (6)). The following lemmas will manipulate and combine Eqs. (5) and (6) in order to establish an upper bound for the time rate of change of the norm.

Lemma 4.1. *For all FR schemes, Eq. (5) holds, and therefore the following results also hold*

$$\frac{J_n}{2} \frac{d}{dt} \int_{\boldsymbol{\Omega}_n} \left(u_n^D\right)^2 d\boldsymbol{\Omega}_n = -\int_{\boldsymbol{\Omega}_S} \hat{u}^D \left(\hat{\nabla} \cdot \hat{\mathbf{f}}^D + \hat{\nabla} \cdot \hat{\mathbf{f}}^C\right) d\boldsymbol{\Omega}_S \tag{48}$$

and

$$\frac{J_n}{2A_S} \frac{d}{dt} \int_{\boldsymbol{\Omega}_n} \left(D^{(m,p)} u_n^D\right)^2 d\boldsymbol{\Omega}_n = -\left(D^{(m,p)} \hat{u}^D\right)\left(D^{(m,p)} \left(\hat{\nabla} \cdot \hat{\mathbf{f}}^C\right)\right). \tag{49}$$

Proof. The following relation holds for all FR schemes: $\nabla \cdot \mathbf{f}_n = \nabla \cdot \mathbf{f}_n^D + \nabla \cdot \mathbf{f}_n^C$. Upon combining this relation and Eq. (5) and rearranging the result, one obtains

$$\frac{\partial u_n^D}{\partial t} = -\nabla \cdot \mathbf{f}_n^D - \nabla \cdot \mathbf{f}_n^C. \tag{50}$$

Multiplying this equation by $J_n u_n^D$ and integrating over the element domain $\boldsymbol{\Omega}_n$ yields the following

$$\frac{J_n}{2} \frac{d}{dt} \int_{\boldsymbol{\Omega}_n} \left(u_n^D\right)^2 d\boldsymbol{\Omega}_n = -\int_{\boldsymbol{\Omega}_n} J_n u_n^D \left(\nabla \cdot \mathbf{f}_n^D\right) d\boldsymbol{\Omega}_n - \int_{\boldsymbol{\Omega}_n} J_n u_n^D \left(\nabla \cdot \mathbf{f}_n^C\right) d\boldsymbol{\Omega}_n. \tag{51}$$

Upon replacing the integrals over the physical domain $\boldsymbol{\Omega}_n$ on the RHS of Eq. (51) with integrals over the reference domain $\boldsymbol{\Omega}_S$ (using the identity from Eq. (14)), one obtains Eq. (48), the first result of Lemma 4.1.

The second result of Lemma 4.1 can be derived as follows. Consider applying the operator $D^{(m,p)}$ to both sides of Eq. (50) in order to obtain

$$\frac{\partial}{\partial t} \left(D^{(m,p)} u_n^D\right) = -D^{(m,p)}\left(\nabla \cdot \mathbf{f}_n^D\right) - D^{(m,p)}\left(\nabla \cdot \mathbf{f}_n^C\right) = -D^{(m,p)}\left(\nabla \cdot \mathbf{f}_n^C\right). \tag{52}$$

Note that $D^{(m,p)}\left(\nabla \cdot \mathbf{f}_n^D\right) = 0$ because $\nabla \cdot \mathbf{f}_n^D$ is at most degree $(p-1)$.

If both sides of Eq. (52) are multiplied by $\left(D^{(m,p)} u_n^D\right)$ and integrated over $\boldsymbol{\Omega}_n$, one obtains

$$\frac{1}{2} \frac{d}{dt} \int_{\boldsymbol{\Omega}_n} \left(D^{(m,p)} u_n^D\right)^2 d\boldsymbol{\Omega}_n = -\int_{\boldsymbol{\Omega}_n} \left(D^{(m,p)} u_n^D\right)\left(D^{(m,p)}\left(\nabla \cdot \mathbf{f}_n^C\right)\right) d\boldsymbol{\Omega}_n. \tag{53}$$

Substituting Eqs. (8) and (12) into Eq. (53) yields

$$\frac{1}{2} \frac{d}{dt} \int_{\boldsymbol{\Omega}_n} \left(D^{(m,p)} u_n^D\right)^2 d\boldsymbol{\Omega}_n = -\int_{\boldsymbol{\Omega}_S} \frac{1}{J_n} \left(D^{(m,p)} \hat{u}^D\right)\left(D^{(m,p)}\left(\hat{\nabla} \cdot \hat{\mathbf{f}}^C\right)\right) d\boldsymbol{\Omega}_S = -\frac{A_S}{J_n}\left(D^{(m,p)} \hat{u}^D\right)\left(D^{(m,p)}\left(\hat{\nabla} \cdot \hat{\mathbf{f}}^C\right)\right). \tag{54}$$

Upon rearranging Eq. (54) one obtains Eq. (49). This completes the proof of Lemma 4.1. □

Lemma 4.2. *For all FR schemes, Eq. (6) holds, and therefore the following results also hold*

$$J_n \int_{\Omega_n} \mathbf{f}_{dif,n}^D \cdot \mathbf{q}_n^D d\Omega_n = \int_{\Omega_S} \hat{\mathbf{f}}_{dif}^D \cdot \left(\hat{\nabla} \hat{u}^D + \hat{\nabla} \hat{u}^C \right) d\Omega_S \tag{55}$$

and

$$\frac{J_n}{A_S} \int_{\Omega_n} \left(D^{(m,p)} \mathbf{f}_{dif,n}^D \right) \cdot \left(D^{(m,p)} \mathbf{q}_n^D \right) d\Omega_n = \left(D^{(m,p)} \hat{\mathbf{f}}_{dif}^D \right) \cdot \left(D^{(m,p)} \left(\hat{\nabla} \hat{u}^C \right) \right). \tag{56}$$

Proof. The following relation holds for all FR schemes: $\nabla u_n = \nabla u_n^D + \nabla u_n^C$. Upon combining this relation and Eq. (6) and rearranging the result, one obtains

$$\mathbf{q}_n^D = \nabla u_n^D + \nabla u_n^C. \tag{57}$$

Taking the dot product of Eq. (57) with $J_n \mathbf{f}_{dif,n}^D$ and integrating over the element domain Ω_n yields

$$J_n \int_{\Omega_n} \mathbf{f}_{dif,n}^D \cdot \mathbf{q}_n^D d\Omega_n = J_n \int_{\Omega_n} \left(\mathbf{f}_{dif,n}^D \cdot \nabla u_n^D \right) d\Omega_n + J_n \int_{\Omega_n} \left(\mathbf{f}_{dif,n}^D \cdot \nabla u_n^C \right) d\Omega_n. \tag{58}$$

Upon transforming the RHS of Eq. (58) to the reference domain using Eq. (15) (with $\mathbf{f}_{dif,n}^D$ and $\hat{\mathbf{f}}_{dif}^D$ in place of $\mathbf{f}_n$ and $\hat{\mathbf{f}}$, and u_n^D and $\hat{u}^D$ (or u_n^C and $\hat{u}^C$) in place of u_n and $\hat{u}$), one obtains Eq. (55), the first result of Lemma 4.2.

The second result of Lemma 4.2 can be derived as follows. Consider applying the operator $D^{(m,p)}$ to both sides of Eq. (57) in order to obtain

$$D^{(m,p)} \mathbf{q}_n^D = D^{(m,p)} \left(\nabla u_n^D \right) + D^{(m,p)} \left(\nabla u_n^C \right) = D^{(m,p)} \left(\nabla u_n^C \right). \tag{59}$$

The term $D^{(m,p)} \left(\nabla u_n^D \right)$ vanishes because ∇u_n^D is of degree $(p-1)$. Taking the dot product of Eq. (59) with $\left(D^{(m,p)} \mathbf{f}_{dif,n}^D \right)$ and integrating over Ω_n yields

$$\int_{\Omega_n} \left(D^{(m,p)} \mathbf{f}_{dif,n}^D \right) \cdot \left(D^{(m,p)} \mathbf{q}_n^D \right) d\Omega_n = \int_{\Omega_n} \left(D^{(m,p)} \mathbf{f}_{dif,n}^D \right) \cdot \left(D^{(m,p)} \left(\nabla u_n^C \right) \right) d\Omega_n. \tag{60}$$

The RHS can be simplified using the following identity

$$\left(D^{(m,p)} \mathbf{f}_{dif,n}^D \right) \cdot \left(D^{(m,p)} \left(\nabla u_n^C \right) \right) = \frac{1}{J_n^2} \left(D^{(m,p)} \hat{\mathbf{f}}_{dif}^D \right) \cdot \left(D^{(m,p)} \left(\hat{\nabla} \hat{u}^C \right) \right) \tag{61}$$

which derives from the vector identities in Eqs. (9) and (10) (with $\mathbf{f}_{dif,n}^D, \hat{\mathbf{f}}_{dif}^D, u_n^C$, and $\hat{u}^C$ in place of $\mathbf{f}_n, \hat{\mathbf{f}}, u_n$, and $\hat{u}$). Upon substituting Eq. (61) into the RHS of Eq. (60), one obtains

$$\int_{\Omega_n} \left(D^{(m,p)} \mathbf{f}_{dif,n}^D \right) \cdot \left(D^{(m,p)} \mathbf{q}_n^D \right) d\Omega_n = \int_{\Omega_n} \frac{1}{J_n^2} \left(D^{(m,p)} \hat{\mathbf{f}}_{dif}^D \right) \cdot \left(D^{(m,p)} \left(\hat{\nabla} \hat{u}^C \right) \right) d\Omega_n = \frac{A_S}{J_n} \left(D^{(m,p)} \hat{\mathbf{f}}_{dif}^D \right) \cdot \left(D^{(m,p)} \left(\hat{\nabla} \hat{u}^C \right) \right). \tag{62}$$

Upon rearranging Eq. (62) one obtains Eq. (56). This completes the proof of Lemma 4.2. □

Lemma 4.3. *If $\phi_{f,j}$ and $\psi_{f,j}$ are the VCJH correction fields, the following identity holds*

$$\frac{J_n}{2} \frac{d}{dt} \int_{\Omega_n} \left(u_n^D \right)^2 d\Omega_n + \frac{J_n}{2A_S} \frac{d}{dt} \int_{\Omega_n} \sum_{m=1}^{p+1} c_m \left(D^{(m,p)} u_n^D \right)^2 d\Omega_n - J_n \int_{\Omega_n} \mathbf{f}_{dif,n}^D \cdot \mathbf{q}_n^D d\Omega_n - \frac{J_n}{A_S} \int_{\Omega_n} \sum_{m=1}^{p+1} \kappa_m \left(D^{(m,p)} \mathbf{f}_{dif,n}^D \right) \cdot \left(D^{(m,p)} \mathbf{q}_n^D \right) d\Omega_n$$

$$= -\int_{\Omega_S} \hat{u}^D \left(\hat{\nabla} \cdot \hat{\mathbf{f}}^D \right) d\Omega_S - \int_{\Gamma_S} \hat{u}^D \left(\hat{\mathbf{f}}^C \cdot \hat{\mathbf{n}} \right) d\Gamma_S - \int_{\Omega_S} \hat{\mathbf{f}}_{dif}^D \cdot \left(\hat{\nabla} \hat{u}^D \right) d\Omega_S - \int_{\Gamma_S} \hat{u}^C \left(\hat{\mathbf{f}}_{dif}^D \cdot \hat{\mathbf{n}} \right) d\Gamma_S, \tag{63}$$

where constants c_m and κ_m are related via Eqs. (42) and (A.3) to constants c and κ, respectively, which parameterize the VCJH correction fields $\phi_{f,j}$ and $\psi_{f,j}$, respectively.

Proof. Consider subtracting Eq. (55) from Eq. (48) in order to obtain

$$\frac{J_n}{2} \frac{d}{dt} \int_{\Omega_n} \left(u_n^D \right)^2 d\Omega_n - J_n \int_{\Omega_n} \mathbf{f}_{dif,n}^D \cdot \mathbf{q}_n^D d\Omega_n = -\int_{\Omega_S} \hat{u}^D \left(\hat{\nabla} \cdot \hat{\mathbf{f}}^D + \hat{\nabla} \cdot \hat{\mathbf{f}}^C \right) d\Omega_S - \int_{\Omega_S} \hat{\mathbf{f}}_{dif}^D \cdot \left(\hat{\nabla} \hat{u}^D + \hat{\nabla} \hat{u}^C \right) d\Omega_S. \tag{64}$$

Next, consider multiplying Eq. (49) by c_m and Eq. (56) by $-\kappa_m$, summing each equation over m, and adding the results to Eq. (64) in order to obtain

$$\frac{J_n}{2} \frac{d}{dt} \int_{\Omega_n} \left(u_n^D \right)^2 d\Omega_n + \frac{J_n}{2A_S} \frac{d}{dt} \int_{\Omega_n} \sum_{m=1}^{p+1} c_m \left(D^{(m,p)} u_n^D \right)^2 d\Omega_n - J_n \int_{\Omega_n} \mathbf{f}_{dif,n}^D \cdot \mathbf{q}_n^D d\Omega_n - \frac{J_n}{A_S} \int_{\Omega_n} \sum_{m=1}^{p+1} \kappa_m \left(D^{(m,p)} \mathbf{f}_{dif,n}^D \right) \cdot \left(D^{(m,p)} \mathbf{q}_n^D \right) d\Omega_n$$

$$= -\int_{\Omega_S} \hat{u}^D \left(\hat{\nabla} \cdot \hat{\mathbf{f}}^D + \hat{\nabla} \cdot \hat{\mathbf{f}}^C \right) d\Omega_S - \sum_{m=1}^{p+1} c_m \left(D^{(m,p)} \hat{u}^D \right) \left(D^{(m,p)} \left(\hat{\nabla} \cdot \hat{\mathbf{f}}^C \right) \right) - \int_{\Omega_S} \hat{\mathbf{f}}_{dif}^D \cdot \left(\hat{\nabla} \hat{u}^D + \hat{\nabla} \hat{u}^C \right) d\Omega_S$$

$$- \sum_{m=1}^{p+1} \kappa_m \left(D^{(m,p)} \hat{\mathbf{f}}_{dif}^D \right) \cdot \left(D^{(m,p)} \left(\hat{\nabla} \hat{u}^C \right) \right). \tag{65}$$

Suppose that $\hat{\nabla} \cdot \hat{\mathbf{f}}^C$ and $\hat{\nabla}\hat{u}^C$ are constructed based on correction fields $\phi_{f,j} = \hat{\nabla} \cdot \mathbf{h}_{f,j}$ and $\psi_{f,j} = \hat{\nabla} \cdot \mathbf{g}_{f,j}$, respectively, which satisfy the following identities (that are satisfied if $\mathbf{h}_{f,j}$ and $\mathbf{g}_{f,j}$ are the VCJH correction functions as shown in [25])

$$\int_{\Omega_S} \mathbf{h}_{f,j} \cdot \hat{\nabla}L_i \, d\Omega_S - \sum_{m=1}^{p+1} c_m \left(D^{(m,p)} L_i \right) \left(D^{(m,p)} \phi_{f,j} \right) = 0, \tag{66}$$

$$\int_{\Omega_S} \mathbf{g}_{f,j} \cdot \hat{\nabla}L_i \, d\Omega_S - \sum_{m=1}^{p+1} \kappa_m \left(D^{(m,p)} L_i \right) \left(D^{(m,p)} \psi_{f,j} \right) = 0. \tag{67}$$

Appendix B shows that if Eqs. (66) and (67) hold, then the following results also hold

$$\sum_{m=1}^{p+1} c_m \left(D^{(m,p)} \hat{u}^D \right) \left(D^{(m,p)} \left(\hat{\nabla} \cdot \hat{\mathbf{f}}^C \right) \right) = \int_{\Gamma_S} \hat{u}^D \left(\hat{\mathbf{f}}^C \cdot \hat{\mathbf{n}} \right) d\Gamma_S - \int_{\Omega_S} \hat{u}^D \left(\hat{\nabla} \cdot \hat{\mathbf{f}}^C \right) d\Omega_S, \tag{68}$$

$$\sum_{m=1}^{p+1} \kappa_m \left(D^{(m,p)} \hat{\mathbf{f}}_{dif}^D \right) \cdot \left(D^{(m,p)} \left(\hat{\nabla}\hat{u}^C \right) \right) = \int_{\Gamma_S} \hat{u}^C \left(\hat{\mathbf{f}}_{dif}^D \cdot \hat{\mathbf{n}} \right) d\Gamma_S - \int_{\Omega_S} \left(\hat{\mathbf{f}}_{dif}^D \cdot \hat{\nabla}\hat{u}^C \right) d\Omega_S. \tag{69}$$

Upon substituting Eqs. (68) and (69) into the RHS of Eq. (65), one obtains Eq. (63). This completes the proof of Lemma 4.3. □

Theorem 4.1. *If the VCJH schemes on triangles (for which Lemmas 4.1–4.3 hold) are employed in conjunction with the Lax–Friedrichs formulation for the advective numerical flux* $\mathbf{f}_{adv}^I$

$$\mathbf{f}_{adv}^I = \{\{\mathbf{f}_{adv}^D\}\} + \frac{\lambda}{2} \left(\max_{u \in [u_-^D, u_+^D]} \left| \frac{\partial \mathbf{f}_{adv}}{\partial u} \cdot \mathbf{n} \right| \right) [\![u^D]\!], \tag{70}$$

with $0 \leqslant \lambda \leqslant 1$, *and the LDG formulation for the common solution* u^I *and diffusive numerical flux* $\mathbf{f}_{dif}^I$,

$$u^I = \{\{u^D\}\} - \beta \cdot [\![u^D]\!], \tag{71}$$

$$\mathbf{f}_{dif}^I = \{\{\mathbf{f}_{dif}^D\}\} + \tau[\![u^D]\!] + \beta[\![\mathbf{f}_{dif}^D]\!], \tag{72}$$

with $\beta = (\beta_x, \beta_y)$ *and* $\tau \geqslant 0$, *then it can be shown that the following result holds*

$$\frac{d}{dt} \|U^D\|_{p,c}^2 \leqslant 0. \tag{73}$$

Proof. The fluxes $\hat{\mathbf{f}}^C$ and $\hat{\mathbf{f}}^D$ in Eq. (63) (from Lemma 4.3) can be expressed in terms of advective and diffusive parts: in particular $\hat{\mathbf{f}}^C = \hat{\mathbf{f}}_{adv}^C + \hat{\mathbf{f}}_{dif}^C$ and $\hat{\mathbf{f}}^D = \hat{\mathbf{f}}_{adv}^D + \hat{\mathbf{f}}_{dif}^D$. In addition, the diffusive flux $\mathbf{f}_{dif,n}$ on the LHS of Eq. (63) is defined such that $\mathbf{f}_{dif,n} = -b\mathbf{q}_n^D$ (as mentioned previously). As a result, Eq. (63) becomes

$$\frac{J_n}{2} \frac{d}{dt} \int_{\Omega_n} \left[(u_n^D)^2 + \frac{1}{A_S} \sum_{m=1}^{p+1} c_m \left(D^{(m,p)} u_n^D \right)^2 \right] d\Omega_n + b J_n \int_{\Omega_n} \left[\mathbf{q}_n^D \cdot \mathbf{q}_n^D + \frac{1}{A_S} \sum_{m=1}^{p+1} \kappa_m \left(D^{(m,p)} \mathbf{q}_n^D \right) \cdot \left(D^{(m,p)} \mathbf{q}_n^D \right) \right] d\Omega_n$$

$$= -\int_{\Omega_S} \hat{u}^D \left(\hat{\nabla} \cdot \hat{\mathbf{f}}_{adv}^D \right) d\Omega_S - \int_{\Gamma_S} \hat{u}^D \left(\hat{\mathbf{f}}_{adv}^C \cdot \hat{\mathbf{n}} \right) d\Gamma_S - \int_{\Omega_S} \hat{u}^D \left(\hat{\nabla} \cdot \hat{\mathbf{f}}_{dif}^D \right) d\Omega_S - \int_{\Omega_S} \left(\hat{\nabla}\hat{u}^D \cdot \hat{\mathbf{f}}_{dif}^D \right) d\Omega_S$$

$$- \int_{\Gamma_S} \hat{u}^D \left(\hat{\mathbf{f}}_{dif}^C \cdot \hat{\mathbf{n}} \right) d\Gamma_S - \int_{\Gamma_S} \hat{u}^C \left(\hat{\mathbf{f}}_{dif}^D \cdot \hat{\mathbf{n}} \right) d\Gamma_S. \tag{74}$$

Setting Eq. (74) aside for the moment, one may consider the following identity

$$\hat{u}^D (\hat{\nabla} \cdot \hat{\mathbf{f}}_{adv}^D) = \frac{1}{2} \hat{\nabla} \cdot (\hat{u}^D \hat{\mathbf{f}}_{adv}^D), \tag{75}$$

which holds because $\hat{\mathbf{f}}_{adv}^D = \mathbf{J}_n^{-1} \mathbf{a} \hat{u}^D$, $\mathbf{J}_n^{-1}$ is a constant matrix, and $\mathbf{a}$ is a constant vector. On substituting Eq. (75) into the RHS of Eq. (74), and employing the divergence theorem and integration by parts, one obtains

$$\frac{J_n}{2} \frac{d}{dt} \int_{\Omega_n} \left[(u_n^D)^2 + \frac{1}{A_S} \sum_{m=1}^{p+1} c_m \left(D^{(m,p)} u_n^D \right)^2 \right] d\Omega_n + b \int_{\Omega_n} \left[\mathbf{q}_n^D \cdot \mathbf{q}_n^D + \frac{1}{A_S} \sum_{m=1}^{p+1} \kappa_m \left(D^{(m,p)} \mathbf{q}_n^D \right) \cdot \left(D^{(m,p)} \mathbf{q}_n^D \right) \right] d\Omega_n$$

$$= -\frac{1}{2} \int_{\Gamma_S} \hat{u}^D \left(\hat{\mathbf{f}}_{adv}^D \cdot \hat{\mathbf{n}} \right) d\Gamma_S - \int_{\Gamma_S} \hat{u}^D \left(\hat{\mathbf{f}}_{adv}^C \cdot \hat{\mathbf{n}} \right) d\Gamma_S - \int_{\Gamma_S} \hat{u}^D \left(\hat{\mathbf{f}}_{dif}^D \cdot \hat{\mathbf{n}} \right) d\Gamma_S - \int_{\Gamma_S} \hat{u}^D \left(\hat{\mathbf{f}}_{dif}^C \cdot \hat{\mathbf{n}} \right) d\Gamma_S - \int_{\Gamma_S} \hat{u}^C \left(\hat{\mathbf{f}}_{dif}^D \cdot \hat{\mathbf{n}} \right) d\Gamma_S. \tag{76}$$

Consider the following identities

$$\hat{u}|_{\Gamma_S} = (\hat{u}^D + \hat{u}^C)\big|_{\Gamma_S} = \hat{u}^I, \quad \hat{\mathbf{f}} \cdot \hat{\mathbf{n}}\big|_{\Gamma_S} = \left(\hat{\mathbf{f}}^D + \hat{\mathbf{f}}^C \right) \cdot \hat{\mathbf{n}}\big|_{\Gamma_S} = \hat{\mathbf{f}}^I \cdot \hat{\mathbf{n}}, \tag{77}$$

where (on each face $\mathbf{\Gamma}_f$)

$$\hat{u}^I = \sum_{j=1}^{N_{fp}} \hat{u}_{f,j}^I \hat{l}_{f,j}^{1D}, \quad \hat{\mathbf{f}}^I = \sum_{j=1}^{N_{fp}} \hat{\mathbf{f}}_{f,j}^I \hat{l}_{f,j}^{1D}, \tag{78}$$

and where each $\hat{l}_{f,j}^{1D}$ is a 1D Lagrange polynomial on face f which assumes the value of 1 at flux point j and assumes the value of 0 at all neighboring flux points. One may use Eq. (77) to eliminate $\hat{\mathbf{f}}^C$ and $\hat{u}^C$ from Eq. (76), and thereafter one may use Eq. (16) to transform the integrals on the RHS in order to obtain the following expression

$$\frac{1}{2}\frac{d}{dt}\int_{\mathbf{\Omega}_n}\left[(u_n^D)^2 + \frac{1}{A_S}\sum_{m=1}^{p+1}c_m\left(D^{(m,p)}u_n^D\right)^2\right]d\mathbf{\Omega}_n + b\int_{\mathbf{\Omega}_n}\left[\mathbf{q}_n^D\cdot\mathbf{q}_n^D + \frac{1}{A_S}\sum_{m=1}^{p+1}\kappa_m\left(D^{(m,p)}\mathbf{q}_n^D\right)\cdot\left(D^{(m,p)}\mathbf{q}_n^D\right)\right]d\mathbf{\Omega}_n$$
$$= \int_{\mathbf{\Gamma}_n}\left[\frac{1}{2}u_n^D\left(\mathbf{f}_{adv,n}^D\cdot\mathbf{n}\right) - u_n^D\left(\mathbf{f}_{adv}^I\cdot\mathbf{n}\right)\right]d\mathbf{\Gamma}_n + \int_{\mathbf{\Gamma}_n}\left[u_n^D\left(\mathbf{f}_{dif,n}^D\cdot\mathbf{n}\right) - u_n^D\left(\mathbf{f}_{dif}^I\cdot\mathbf{n}\right) - u^I\left(\mathbf{f}_{dif,n}^D\cdot\mathbf{n}\right)\right]d\mathbf{\Gamma}_n, \tag{79}$$

where the quantities u^I, $\mathbf{f}_{adv}^I$, and $\mathbf{f}_{dif}^I$ are defined (on each face $\mathbf{\Gamma}_f$) as

$$u^I = \sum_{j=1}^{N_{fp}} u_{f,j}^I l_{f,j}^{1D}, \quad \mathbf{f}_{adv}^I = \sum_{j=1}^{N_{fp}} \mathbf{f}_{(f,j)\,adv}^I l_{f,j}^{1D}, \quad \mathbf{f}_{dif}^I = \sum_{j=1}^{N_{fp}} \mathbf{f}_{(f,j)\,dif}^I l_{f,j}^{1D}. \tag{80}$$

To obtain a description of the solution behavior within the entire domain, one must sum over all the elements in the mesh (summing over n on Eq. (79)) as follows

$$\frac{1}{2}\frac{d}{dt}\sum_{n=1}^{N}\left\{\int_{\mathbf{\Omega}_n}\left[(u_n^D)^2 + \frac{1}{A_S}\sum_{m=1}^{p+1}c_m\left(D^{(m,p)}u_n^D\right)^2\right]d\mathbf{\Omega}_n\right\} + b\sum_{n=1}^{N}\left\{\int_{\mathbf{\Omega}_n}\left[\mathbf{q}_n^D\cdot\mathbf{q}_n^D + \frac{1}{A_S}\sum_{m=1}^{p+1}\kappa_m\left(D^{(m,p)}\mathbf{q}_n^D\right)\cdot\left(D^{(m,p)}\mathbf{q}_n^D\right)\right]d\mathbf{\Omega}_n\right\}$$
$$= \sum_{n=1}^{N}\left\{\int_{\mathbf{\Gamma}_n}\left[\frac{1}{2}u_n^D\left(\mathbf{f}_{adv,n}^D\cdot\mathbf{n}\right) - u_n^D\left(\mathbf{f}_{adv}^I\cdot\mathbf{n}\right)\right]d\mathbf{\Gamma}_n\right\} + \sum_{n=1}^{N}\left\{\int_{\mathbf{\Gamma}_n}\left[u_n^D\left(\mathbf{f}_{dif,n}^D\cdot\mathbf{n}\right) - u_n^D\left(\mathbf{f}_{dif}^I\cdot\mathbf{n}\right) - u^I\left(\mathbf{f}_{dif,n}^D\cdot\mathbf{n}\right)\right]d\mathbf{\Gamma}_n\right\}. \tag{81}$$

For constants c_m and κ_m that satisfy $0 \leqslant c_m < \infty$ and $0 \leqslant \kappa_m < \infty$, the expressions

$$\|U^D\|_{p,c} = \left\{\sum_{n=1}^{N}\int_{\mathbf{\Omega}_n}\left[(u_n^D)^2 + \frac{1}{A_S}\sum_{m=1}^{p+1}c_m\left(D^{(m,p)}u_n^D\right)^2\right]d\mathbf{\Omega}_n\right\}^{1/2} \tag{82}$$

and

$$\|\mathbf{Q}^D\|_{p,\kappa} = \left\{\sum_{n=1}^{N}\int_{\mathbf{\Omega}_n}\left[\mathbf{q}_n^D\cdot\mathbf{q}_n^D + \frac{1}{A_S}\sum_{m=1}^{p+1}\kappa_m\left(D^{(m,p)}\mathbf{q}_n^D\right)\cdot\left(D^{(m,p)}\mathbf{q}_n^D\right)\right]d\mathbf{\Omega}_n\right\}^{1/2} \tag{83}$$

are broken Sobolev-type norms of the solution U^D and the auxiliary variable $\mathbf{Q}^D$, respectively. The expressions

$$\Theta_{adv} = \sum_{n=1}^{N}\left\{\int_{\mathbf{\Gamma}_n}\left[\frac{1}{2}u_n^D\left(\mathbf{f}_{adv,n}^D\cdot\mathbf{n}\right) - u_n^D\left(\mathbf{f}_{adv}^I\cdot\mathbf{n}\right)\right]d\mathbf{\Gamma}_n\right\} \tag{84}$$

and

$$\Theta_{dif} = \sum_{n=1}^{N}\left\{\int_{\mathbf{\Gamma}_n}\left[u_n^D\left(\mathbf{f}_{dif,n}^D\cdot\mathbf{n}\right) - u_n^D\left(\mathbf{f}_{dif}^I\cdot\mathbf{n}\right) - u^I\left(\mathbf{f}_{dif,n}^D\cdot\mathbf{n}\right)\right]d\mathbf{\Gamma}_n\right\} \tag{85}$$

represent contributions from the advective and diffusive fluxes at the element boundaries. Using Eqs. (82)–(85), Eq. (81) can be rewritten as

$$\frac{1}{2}\frac{d}{dt}\|U^D\|_{p,c}^2 = -b\|\mathbf{Q}^D\|_{p,\kappa}^2 + \Theta_{adv} + \Theta_{dif}. \tag{86}$$

On the RHS of Eq. (86), the term $-b\|\mathbf{Q}^D\|_{p,\kappa}^2$ is guarenteed to be non-positive for $b \geqslant 0$, and the terms Θ_{adv} and Θ_{dif} are guaranteed to be non-positive for appropriate choices of the common solution u^I, and the common numerical fluxes $\mathbf{f}_{adv}^I$ and $\mathbf{f}_{dif}^I$.

The Lax–Friedrichs formulation provides a suitable expression for $\mathbf{f}_{adv}^I$ (Eq. (70)). Upon substituting $\mathbf{f}_{adv} = \mathbf{a}u$ into Eq. (70) and taking the dot product with $\mathbf{n}$, one obtains

$$\mathbf{f}_{adv}^I\cdot\mathbf{n} = \left(\{\{\mathbf{a}u^D\}\} + \frac{\lambda}{2}|\mathbf{a}\cdot\mathbf{n}|[\![u^D]\!]\right)\cdot\mathbf{n} = \frac{1}{2}\left(u_+^D + u_-^D\right)(a_x n_x + a_y n_y) + \frac{\lambda}{2}|a_x n_x + a_y n_y|(u_-^D - u_+^D), \tag{87}$$

where (on each face $\mathbf{\Gamma}_f$)

$$u_+^D = \sum_{j=1}^{N_{fp}} u_{(f,j)+}^D \, l_{f,j}^{1D}, \quad u_-^D = \sum_{j=1}^{N_{fp}} u_{(f,j)-}^D \, l_{f,j}^{1D},$$

(88)

and where λ is an upwinding parameter in the sense that $\lambda > 0$ results in an upwind biased flux and $\lambda = 0$ results in a central flux. Castonguay et al. [25] demonstrated that this choice for $\mathbf{f}_{adv}^I$ ensures $\Theta_{adv} \leqslant 0$.

The LDG formulation provides suitable expressions for u^I and $\mathbf{f}_{dif}^I$ (Eqs. (71) and (72)). Upon expanding Eq. (71), one obtains

$$u^I = \{\{u^D\}\} - \beta \cdot [\![u^D]\!] = \frac{1}{2}\left(u_-^D + u_+^D\right) - \left(u_-^D - u_+^D\right)\left(\beta_x n_x + \beta_y n_y\right),$$

(89)

and upon substituting $\mathbf{f}_{dif} = -b\mathbf{q}$ into Eq. (72) and taking the dot product with $\mathbf{n}$, one obtains

$$
\begin{aligned}
\mathbf{f}_{dif}^I \cdot \mathbf{n} &= \left(\{\{\mathbf{f}_{dif}^D\}\} + \tau[\![u^D]\!] + \beta[\![\mathbf{f}_{dif}^D]\!]\right) \cdot \mathbf{n} \\
&= -b\left[\frac{1}{2}\left(q_{x-}^D + q_{x+}^D\right)n_x + \frac{1}{2}\left(q_{y-}^D + q_{y+}^D\right)n_y\right. \\
&\quad \left. + \left(\left(q_{x-}^D - q_{x+}^D\right)n_x + \left(q_{y-}^D - q_{y+}^D\right)n_y\right)\left(\beta_x n_x + \beta_y n_y\right)\right] + \tau\left(u_-^D - u_+^D\right),
\end{aligned}
$$

(90)

where (on each face Γ_f)

$$\begin{bmatrix} q_{x+}^D \\ q_{y+}^D \end{bmatrix} = \mathbf{q}_+^D = \sum_{j=1}^{N_{fp}} \mathbf{q}_{(f,j)+}^D \, l_{f,j}^{1D}, \quad \begin{bmatrix} q_{x-}^D \\ q_{y-}^D \end{bmatrix} = \mathbf{q}_-^D = \sum_{j=1}^{N_{fp}} \mathbf{q}_{(f,j)-}^D \, l_{f,j}^{1D}.$$

(91)

In what follows, it will be shown that this choice for u^I and $\mathbf{f}_{dif}^I$ ensures $\Theta_{dif} \leqslant 0$.

On substituting Eqs. (89) and (90) into the combination of Eqs. (85) and (86), and replacing u_n^D and $\mathbf{q}_n^D$ with u_-^D and $\mathbf{q}_-^D = (q_{x-}^D, q_{y-}^D)$, respectively, one obtains

$$
\begin{aligned}
\frac{1}{2}\frac{d}{dt}\|U^D\|_{p,c}^2 &= -b\|\mathbf{Q}^D\|_{p,\kappa}^2 + \Theta_{adv} + \sum_{n=1}^{N}\Bigg\{\int_{\Gamma_n}\Bigg[b\left(\frac{u_-^D}{2}\left(q_{x+}^D n_x + q_{y+}^D n_y\right) + \frac{u_+^D}{2}\left(q_{x-}^D n_x + q_{y-}^D n_y\right) + \left(u_+^D\left(q_{x-}^D n_x + q_{y-}^D n_y\right)\right.\right. \\
&\quad \left.\left. - u_-^D\left(q_{x+}^D n_x + q_{y+}^D n_y\right)\right)\left(\beta_x n_x + \beta_y n_y\right)\right) + \tau\left(u_-^D u_+^D - (u_-^D)^2\right)\Bigg]d\Gamma_n\Bigg\}.
\end{aligned}
$$

(92)

The last term on the RHS of Eq. (92) can be rewritten as a sum over edges instead of a sum over elements. Assuming the domain is such that periodic boundary conditions can be imposed, each edge receives contributions from two adjacent elements. Using the notation $u_{e,+}^D, q_{x_{e,+}}^D, q_{y_{e,+}}^D$ and $u_{e,-}^D, q_{x_{e,-}}^D, q_{y_{e,-}}^D$ to define the solution and auxiliary variable from the elements on the right and left sides of an edge, respectively, Eq. (92) becomes

$$
\begin{aligned}
\frac{1}{2}\frac{d}{dt}\|U^D\|_{p,c}^2 &= -b\|\mathbf{Q}^D\|_{p,\kappa}^2 + \Theta_{adv} + \sum_{e=1}^{N_e}\Bigg\{\int_{\Gamma_e}\Bigg[b\left(\frac{u_{e,-}^D}{2}\left(q_{x_{e,+}}^D n_x + q_{y_{e,+}}^D n_y\right) + \frac{u_{e,+}^D}{2}\left(q_{x_{e,-}}^D n_x + q_{y_{e,-}}^D n_y\right)\right. \\
&\quad -\frac{u_{e,+}^D}{2}\left(q_{x_{e,-}}^D n_x + q_{y_{e,-}}^D n_y\right) - \frac{u_{e,-}^D}{2}\left(q_{x_{e,+}}^D n_x + q_{y_{e,+}}^D n_y\right) + \left(u_{e,-}^D\left(q_{x_{e,+}}^D n_x + q_{y_{e,+}}^D n_y\right) - u_{e,+}^D\left(q_{x_{e,-}}^D n_x + q_{y_{e,-}}^D n_y\right)\right)\left(\beta_x n_x + \beta_y n_y\right) \\
&\quad + \left(u_{e,+}^D\left(q_{x_{e,-}}^D n_x + q_{y_{e,-}}^D n_y\right) - u_{e,-}^D\left(q_{x_{e,+}}^D n_x + q_{y_{e,+}}^D n_y\right)\right)\left(\beta_x n_x + \beta_y n_y\right) + \tau\left(u_{e,-}^D u_{e,+}^D - (u_{e,-}^D)^2\right) \\
&\quad \left. + \tau\left(u_{e,+}^D u_{e,-}^D - (u_{e,+}^D)^2\right)\right]d\Gamma_e\Bigg\} = -b\|\mathbf{Q}^D\|_{p,\kappa}^2 + \Theta_{adv} - \tau\sum_{e=1}^{N_e}\Bigg\{\int_{\Gamma_e}\left(u_{e,+}^D - u_{e,-}^D\right)^2 d\Gamma_e\Bigg\}.
\end{aligned}
$$

(93)

In the equation above, Γ_e represents edge e. Eq. (73) follows immediately from Eq. (93) because $b \geqslant 0$, $\tau \geqslant 0$, and $\Theta_{adv} \leqslant 0$ from [25]. This completes the proof of Theorem 4.1. $\square$

Remark. Theorem 4.1 guarantees the stability of VCJH schemes for linear advection–diffusion problems on triangles. In summary, this theorem was obtained assuming that:

1. The approximate solution U^D is computed on a domain of straight-sided triangles, each with a constant value of J_n.
2. The correction functions ($\mathbf{g}_{f,j}$ and $\mathbf{h}_{f,j}$) and fields ($\psi_{f,j}$ and $\phi_{f,j}$) are the VCJH correction functions and fields defined in Section 3 and Appendix A. This ensures that Eqs. (68) and (69) are satisfied, constants c and κ are non-negative, and thus $\|U^D\|_{p,c}$ and $\|\mathbf{Q}^D\|_{p,\kappa}$ are norms.
3. The advective numerical flux is computed using the Lax–Friedrichs approach (Eq. (87)).
4. The common solution and diffusive numerical flux are computed using the LDG approach (Eqs. (89) and (90)).

Note that, the stability proof has been constructed for the specific case in which the Lax–Friedrichs approach is used for the advective numerical flux and the LDG approach is used for the common solution and diffusive numerical flux. However, the proof still has broad applicability because the Lax–Friedrichs approach recovers the central and upwind approaches, and the LDG approach recovers the BR1 and CF approaches. Furthermore, it appears that the proof can be extended to alternative flux formulations, in particular to compact approaches such as the CDG, BR2, or IP approaches. However, such extensions are beyond the scope of this article because, as discussed previously, this article is concerned with demonstrating the favorable performance of VCJH discretizations paired with explicit time-stepping approaches, for which compactness is not necessarily essential.

5. Linear numerical experiments

This section will investigate the orders of accuracy and explicit time-step limits associated with the VCJH schemes on triangles by performing numerical experiments to solve the linear advection–diffusion equation.

Consider the 2D, time-dependent, linear advection–diffusion of a scalar $u = u(\mathbf{x}, t)$ governed by Eqs. (46) and (47) in the square domain $[-1, 1] \times [-1, 1]$, subject to a sinusoidal initial condition $u(\mathbf{x}, 0) = \sin(\pi x)\sin(\pi y)$, and periodic boundary conditions. The exact solution takes the form

$$u^e = \exp\left(-2b\pi^2 t\right) \sin\left(\pi(x - a_x t)\right) \sin\left(\pi(y - a_y t)\right), \tag{94}$$

where $a_x = a\cos\theta$ and $a_y = a\sin\theta$ are the wave speeds in the x and y directions, and b is the diffusivity coefficient. Numerical experiments were performed on two variants of this problem: a diffusion problem with $a = 0$ and $b = 0.1$, and an advection–diffusion problem with $a = 1$, $b = 0.1$, and $\theta = \pi/6$. These problems were solved using the VCJH schemes in conjunction with a Lax–Friedrichs formulation for the advective numerical flux and a LDG formulation for the common solution and diffusive numerical flux. The schemes were marched forward in time from $t = 0$ to $t = 1$ using an explicit, low-storage, 5-stage, 4th order Runge–Kutta scheme for time advancement (denoted RK54) [37]. For the order of accuracy analysis, the time-step was chosen sufficiently small to ensure that temporal errors were negligible relative to spatial errors.

In the experiments, VCJH schemes parameterized by c and κ were paired with Lax–Friedrichs fluxes parameterized by λ and LDG fluxes parameterized by β and τ. Values of c, κ, λ, β, and τ were selected as follows:

- Choosing c and κ: Four values of c, (namely, c_{dg}, c_{sd}, c_{hu}, and c_+), have been shown to produce favorable results for advection problems on triangles [38]. For advection problems on triangles, Castonguay et al. [38,25] demonstrated that c_{dg} recovers a collocation-based nodal DG scheme (as mentioned previously), c_{sd} and c_{hu} recover schemes with properties similar to the one-dimensional SD scheme [20] and Huynh's $g2$ scheme [6], and finally c_+ recovers a scheme which yields a maximum explicit time-step limit. In the experiments documented in this paper, these four values of c were paired with four equivalent values of κ, namely, $\kappa = \kappa_{dg} = c_{dg}$, $\kappa = \kappa_{sd} = c_{sd}$, $\kappa = \kappa_{hu} = c_{hu}$, and $\kappa = \kappa_+ = c_+$. Table 1 shows the numerical values of c and κ for polynomial orders $p = 2$ and $p = 3$, for several different time-stepping schemes, including the RK54 time-stepping scheme.
  Note that the experiments did not utilize values of c and κ that were larger than c_+ and κ_+, as it has been shown that choosing $c \gg c_+$ and $\kappa \gg \kappa_+$ results in a significant reduction in the order of accuracy of VCJH schemes for 1D advection–diffusion problems [23].
- Choosing λ: All of the numerical experiments were performed with $\lambda = 1$. This value of λ ensures that the advective numerical flux is computed using information exclusively from the upwind direction.
- Choosing β: All of the numerical experiments were performed with $\beta = \pm 0.5\mathbf{n}_-$. This value of β promotes compactness of the scheme (as mentioned previously) [29,30].

Table 1
Reference values of c and κ for $p = 2$ and $p = 3$, for the 3-stage, 3rd order Runge–Kutta scheme (RK33), the 4-stage, 4th order, Runge–Kutta scheme (RK44), and a 5-stage, 4th order, Runge–Kutta scheme (RK54) [37]. These values were computed using von Neumann analysis (similar to the analysis performed in [25]) of the VCJH schemes on uniform grids of right triangular elements.

		$p = 2$	$p = 3$
RK33	$c_{dg} = \kappa_{dg}$	0	0
	$c_{sd} = \kappa_{sd}$	3.75e−03	1.23e−04
	$c_{hu} = \kappa_{hu}$	8.45e−03	2.19e−04
	$c_+ = \kappa_+$	2.61e−02	4.92e−04
RK44	$c_{dg} = \kappa_{dg}$	0	0
	$c_{sd} = \kappa_{sd}$	3.51e−03	1.13e−04
	$c_{hu} = \kappa_{hu}$	7.90e−03	2.01e−04
	$c_+ = \kappa_+$	2.44e−02	4.50e−04
RK54	$c_{dg} = \kappa_{dg}$	0	0
	$c_{sd} = \kappa_{sd}$	4.50e−03	1.17e−04
	$c_{hu} = \kappa_{hu}$	1.01e−02	2.08e−04
	$c_+ = \kappa_+$	3.13e−02	4.67e−04

- Choosing τ: All numerical experiments were performed with $\tau = 0.1$. This value of τ has been shown to yield favorable results for linear advection–diffusion problems in 1D [23].

5.1. Orders of accuracy and explicit time step limits

The orders of accuracy were evaluated on regular triangular meshes created by dividing cartesian $\bar{N} \times \bar{N}$ quadrilateral meshes into meshes with $N = 2\bar{N}^2$ triangular elements. Triangular meshes with $\bar{N} = 16, 24, 32, 48, 64, 96, 128$, and 192 were created. On each mesh, errors in the solution and the solution gradient were measured using the following L2 norm and seminorm

$$E^{(L2)} = \sqrt{\sum_{n=1}^{N} \int_{\Omega_n} (u^e - u_n^D)^2 \, d\Omega_n}, \tag{95}$$

$$E^{(L2s)} = \sqrt{\sum_{n=1}^{N} \int_{\Omega_n} \left[\left(\frac{\partial u^e}{\partial x} - \frac{\partial u_n^D}{\partial x} \right)^2 + \left(\frac{\partial u^e}{\partial y} - \frac{\partial u_n^D}{\partial y} \right)^2 \right] d\Omega_n}. \tag{96}$$

In Eqs. (95) and (96), the integrals over each element domain Ω_n were computed using a quadrature rule of sufficient strength. The expected order of accuracy for $E^{(L2)}$ was $p + 1$, and the expected order for $E^{(L2s)}$ was p, where h was the mesh spacing. A single, representative value for each order of accuracy was determined using a linear least-squares fit of the error vs. the mesh spacing on a log scale. For each least-squares curve fit, the correlation coefficient was greater than 0.999.

In addition to orders of accuracy, explicit time-step limits were obtained for the VCJH schemes. The explicit time-step limit for each scheme was determined by using an iterative method to find the largest time-step that allowed the solution to remain bounded at $t = 1$.

For each of the schemes, Tables 2–4 contain values of the time-step limit and the absolute error obtained on the grid with $\bar{N} = 32$, along with the order of accuracy obtained on the sequence of grids described above. In particular, Tables 2 and 3 show the results for the diffusion problem, where the order of accuracy was obtained on grids with $\bar{N} = 24, 32, 48, 64, 96, 128$, and 192 for $p = 2$ and $\bar{N} = 16, 24, 32, 48, 64, 96$, and 128 for $p = 3$. Table 4 shows the results for the advection–diffusion problem, where the order of accuracy was obtained on grids with $\bar{N} = 16, 24, 32, 48, 64, 96$, and 128 for $p = 3$. Note that the results for the diffusion and the advection–diffusion problems were similar, and thus limited results (only the results for $p = 3$) are shown for the advection–diffusion problem.

The data in Tables 2–4 demonstrates that each scheme obtains the expected order of accuracy. In addition, the data demonstrates that schemes with larger values of c and κ have larger maximum time-steps. The best time-step improvements are shown in Table 2 for $p = 2$, $c = c_+$, and $\kappa = \kappa_+$, where the maximum time-step is approximately 2.2 times larger than that of the collocation-based nodal DG scheme.

5.2. Summary of linear numerical experiments

It has been shown that schemes with small or moderate values of c and κ ($c \lesssim c_+$ and $\kappa \lesssim \kappa_+$) obtain the expected order of accuracy for linear advection–diffusion problems on triangles. In particular, Tables 2–4 show that the VCJH schemes with $c = c_{dg}, c_{sd}, c_{hu}$, or c_+ and $\kappa = \kappa_{dg}, \kappa_{sd}, \kappa_{hu}$, or κ_+, paired with the Lax–Friedrichs flux (with $\lambda = 1$) and the LDG flux (with

Table 2
VCJH scheme accuracy properties and explicit time-step limits for the model linear advection–diffusion problem on triangles with $a = 0$, $b = 0.1$, and $p = 2$. Values of $\lambda = 1$, $\beta = \pm 0.5\mathbf{n}_-$, and $\tau = 0.1$ were used in the experiments. The time-step limit (Δt_{max}) and absolute errors (L_2 and L_{2s} err.) were obtained on the grid with $\bar{N} = 32$.

c	κ	L_2 err.	$O(L_2)$	L_{2s} err.	$O(L_{2s})$	Δt_{max}
c_{dg}	κ_{dg}	1.26e−05	3.00	1.29e−03	2.00	3.18e−04
	κ_{sd}	1.27e−05	3.00	1.22e−03	2.00	3.77e−04
	κ_{hu}	1.33e−05	3.00	1.19e−03	2.00	4.05e−04
	κ_+	1.72e−05	2.99	1.17e−03	2.00	4.51e−04
c_{sd}	κ_{dg}	1.25e−05	3.00	1.29e−03	2.00	3.75e−04
	κ_{sd}	1.27e−05	3.00	1.22e−03	2.00	4.37e−04
	κ_{hu}	1.33e−05	3.00	1.19e−03	2.00	4.76e−04
	κ_+	1.72e−05	2.99	1.17e−03	2.00	5.42e−04
c_{hu}	κ_{dg}	1.25e−05	3.00	1.30e−03	2.00	4.02e−04
	κ_{sd}	1.27e−05	3.00	1.22e−03	2.00	4.73e−04
	κ_{hu}	1.33e−05	3.00	1.19e−03	2.00	5.22e−04
	κ_+	1.72e−05	2.99	1.17e−03	2.00	6.04e−04
c_+	κ_{dg}	1.25e−05	3.00	1.30e−03	2.00	4.42e−04
	κ_{sd}	1.27e−05	3.00	1.22e−03	2.00	5.33e−04
	κ_{hu}	1.34e−05	3.00	1.19e−03	2.00	5.97e−04
	κ_+	1.74e−05	3.00	1.18e−03	2.00	7.07e−04

Table 3
VCJH scheme accuracy properties and explicit time-step limits for the model linear advection–diffusion problem on triangles with $a = 0$, $b = 0.1$, and $p = 3$. Values of $\lambda = 1$, $\beta = \pm 0.5\mathbf{n}_-$, and $\tau = 0.1$ were used in the experiments. The time-step limit (Δt_{max}) and absolute errors (L_2 and L_{2s} err.) were obtained on the grid with $\bar{N} = 32$.

c	κ	L_2 err.	$O(L_2)$	L_{2s} err.	$O(L_{2s})$	Δt_{max}
c_{dg}	κ_{dg}	2.63e−07	4.00	3.54e−05	3.00	1.23e−04
	κ_{sd}	2.68e−07	4.00	3.46e−05	3.00	1.44e−04
	κ_{hu}	2.75e−07	4.00	3.42e−05	3.00	1.50e−04
	κ_+	3.04e−07	3.99	3.34e−05	3.00	1.58e−04
c_{sd}	κ_{dg}	2.63e−07	4.00	3.54e−05	3.00	1.45e−04
	κ_{sd}	2.68e−07	4.00	3.46e−05	3.00	1.64e−04
	κ_{hu}	2.75e−07	4.00	3.42e−05	3.00	1.72e−04
	κ_+	3.04e−07	3.99	3.34e−05	3.00	1.84e−04
c_{hu}	κ_{dg}	2.63e−07	4.00	3.54e−05	3.00	1.51e−04
	κ_{sd}	2.68e−07	4.00	3.46e−05	3.00	1.71e−04
	κ_{hu}	2.75e−07	4.00	3.42e−05	3.00	1.79e−04
	κ_+	3.04e−07	3.99	3.34e−05	3.00	1.93e−04
c_+	κ_{dg}	2.63e−07	4.00	3.54e−05	3.00	1.58e−04
	κ_{sd}	2.68e−07	4.00	3.46e−05	3.00	1.83e−04
	κ_{hu}	2.75e−07	4.00	3.42e−05	3.00	1.92e−04
	κ_+	3.05e−07	4.00	3.34e−05	3.00	2.07e−04

Table 4
VCJH scheme accuracy properties and explicit time-step limits for the model linear advection–diffusion problem on triangles with $a = 1$, $b = 0.1$, and $p = 3$. Values of $\lambda = 1$, $\beta = \pm 0.5\mathbf{n}_-$, and $\tau = 0.1$ were used in the experiments. The time-step limit (Δt_{max}) and absolute errors (L_2 and L_{2s} err.) were obtained on the grid with $\bar{N} = 32$.

c	κ	L_2 err.	$O(L_2)$	L_{2s} err.	$O(L_{2s})$	Δt_{max}
c_{dg}	κ_{dg}	2.62e−07	4.00	3.55e−05	2.99	1.22e−04
	κ_{sd}	2.66e−07	3.99	3.47e−05	2.99	1.43e−04
	κ_{hu}	2.71e−07	3.99	3.43e−05	2.99	1.48e−04
	κ_+	2.92e−07	3.96	3.36e−05	2.99	1.57e−04
c_{sd}	κ_{dg}	2.62e−07	4.00	3.55e−05	2.99	1.43e−04
	κ_{sd}	2.65e−07	3.99	3.47e−05	2.99	1.62e−04
	κ_{hu}	2.70e−07	3.99	3.43e−05	2.99	1.69e−04
	κ_+	2.89e−07	3.96	3.35e−05	2.99	1.82e−04
c_{hu}	κ_{dg}	2.62e−07	4.00	3.55e−05	2.99	1.49e−04
	κ_{sd}	2.65e−07	3.99	3.47e−05	2.99	1.69e−04
	κ_{hu}	2.69e−07	3.98	3.43e−05	2.99	1.77e−04
	κ_+	2.87e−07	3.96	3.35e−05	2.99	1.90e−04
c_+	κ_{dg}	2.62e−07	4.00	3.55e−05	2.99	1.57e−04
	κ_{sd}	2.64e−07	3.99	3.47e−05	2.99	1.81e−04
	κ_{hu}	2.68e−07	3.98	3.43e−05	2.99	1.89e−04
	κ_+	2.82e−07	3.95	3.36e−05	2.99	2.04e−04

$\beta = \pm 0.5\mathbf{n}_-$ and $\tau = 0.1$), recover the expected order of accuracy. In addition, a number of these schemes possess time-step limits which are more than 2 times larger than that of the collocation-based nodal DG scheme.

Finally, although the results of experiments on triangles indicate favorable performance for schemes in which both $\kappa = c$ and $\kappa \neq c$, for simplicity, the authors recommend schemes on triangles for which $\kappa = c$, i.e., schemes which involve pairing κ_{dg} with c_{dg}, κ_{sd} with c_{sd}, κ_{hu} with c_{hu}, or κ_+ with c_+.

6. Nonlinear numerical experiments

Numerical experiments were performed using the Navier–Stokes (NS) equations to determine if the findings of the previous section extended to nonlinear problems. The NS equations can be written as follows

$$\frac{\partial U}{\partial t} + \nabla \cdot \mathbf{F}(U, \nabla U) = 0, \tag{97}$$

where U represents the conserved variables and $\mathbf{F}$ is the flux vector. The conserved variables are defined as $U = \{\rho, \rho u, \rho v, E\}$, where $\rho = \rho(x, y, t)$ is the density, $u = u(x, y, t)$ and $v = v(x, y, t)$ are the velocity components, $E = p/(\gamma - 1) + (1/2)\rho(u^2 + v^2)$ is the total energy, $p = p(x, y, t)$ is the pressure, and γ is the ratio of specific heats. The flux vector $\mathbf{F}$ is composed from inviscid and viscous parts: $\mathbf{F} = \mathbf{F}_{inv}(U) - \mathbf{F}_{visc}(U, \nabla U)$ where $\mathbf{F}_{inv} = (f_{inv}, g_{inv})$ and $\mathbf{F}_{visc} = (f_{visc}, g_{visc})$. The inviscid flux components are defined such that

$$f_{inv} = \begin{Bmatrix} \rho u \\ \rho u^2 + p \\ \rho u v \\ u(E+p) \end{Bmatrix}, \quad g_{inv} = \begin{Bmatrix} \rho v \\ \rho u v \\ \rho v^2 + p \\ v(E+p) \end{Bmatrix}, \tag{98}$$

and the viscous flux components are defined such that

$$f_{visc} = \mu \begin{Bmatrix} 0 \\ 2u_x + \lambda(u_x + v_y) \\ v_x + u_y \\ u[2u_x + \lambda(u_x + v_y)] + v(v_x + u_y) + \frac{C_p}{P_r}T_x \end{Bmatrix},$$

$$g_{visc} = \mu \begin{Bmatrix} 0 \\ v_x + u_y \\ 2v_y + \lambda(u_x + v_y) \\ v[2v_y + \lambda(u_x + v_y)] + u(v_x + u_y) + \frac{C_p}{P_r}T_y \end{Bmatrix}, \tag{99}$$

where μ is the dynamic viscosity, λ is the bulk viscosity coefficient, $T = p/(\rho R)$ is the temperature, R is the gas constant, C_p is the specific heat capacity at constant pressure, and P_r is the Prandtl number. In the viscous flux components, the terms with subscripts x and y signify first derivatives in x and y (for example $T_y = \frac{\partial T}{\partial y}$). These terms arise from the dependence of $\mathbf{F}_{visc}$ on ∇U. Following the approach of Section 2, ∇U can be eliminated and replaced by the auxiliary vector denoted by Q,

$$\frac{\partial U}{\partial t} + \nabla \cdot \mathbf{F}(U, Q) = 0, \tag{100}$$

$$Q - \nabla U = 0. \tag{101}$$

This operation eliminates second derivatives from the NS equations, and reduces them to a first-order system.

6.1. Couette flow

In what follows, the VCJH schemes are used to solve the NS equations for the 'Couette flow' problem. Couette flow occurs between two infinite walls which are unbounded in the $x-z$ plane, and separated by a distance of H in the y direction. One wall is stationary with a temperature of T_w, and the other wall moves in the x direction with a speed of U_w and (the same) temperature of T_w. For $\mu = const$, the flow has an analytical solution where $p = const$ and the total energy E takes the following form

$$E = p\left[\frac{1}{\gamma - 1} + \frac{\frac{Uw^2}{2R}\left(\frac{y}{H}\right)^2}{T_w + \frac{P_r U_w^2}{2C_p}\left(\frac{y}{H}\right)\left[1 - \left(\frac{y}{H}\right)\right]}\right]. \tag{102}$$

It is common practice to generate approximate solutions for Couette flow on finite domains with periodic boundary conditions imposed. In following this approach, experiments were performed on the rectangular domain $[-1, 1] \times [0, 1]$, with periodic conditions imposed on the left and right boundaries, and isothermal wall conditions imposed on the upper and lower boundaries. For the upper and lower isothermal walls, the temperature was given the value of $T = T_w = 300$ K and the pressure was held constant. In addition, no-slip conditions were imposed on the lower wall, i.e., the velocity components on the lower wall were given the values $u = 0$ and $v = 0$. Similarly, no-slip conditions were imposed on the upper wall (which was required to move at a speed of U_w in the x direction), i.e., the velocity components on the upper wall were given the values $u = U_w$ and $v = 0$.

The boundary conditions (described above) were enforced on discretizations of the rectangular domain. The rectangular domain was discretized by forming $2\tilde{N} \times \tilde{N}$ regular quadrilateral meshes and then splitting these meshes into grids with $N = 4\tilde{N}^2$ triangle elements. In this manner, structured grids with $\tilde{N} = 2, 4, 8$, and 16 were formed. In addition, a complementary set of unstructured triangular grids with $N = 16, 64, 256$, and 1024 elements was formed. Fig. 4 shows examples of the structured and unstructured triangular grids for the cases of $\tilde{N} = 4$ and $N = 64$, respectively.

At time $t = 0$, the flow on each domain was initialized with parameters $P_r = 0.72$ and $\gamma = 1.4$, and with velocity components $u = U_w$ and $v = 0$, where U_w was chosen such that the Mach number $M = 0.2$, and the Reynolds number (based on H) was 200. The solution was marched forward in time using the RK54 approach and, at each time-step, the inviscid and viscous numerical fluxes were computed using the Rusanov approach (with $\lambda = 1$) and the LDG approach (with $\beta = \pm 0.5\mathbf{n}_-$ and $\tau = 0.1$). Each simulation was terminated after the residual reached machine zero. Results were obtained on the aforementioned structured and unstructured grids for polynomial orders $p = 2$ and 3, for four different VCJH schemes defined by the following pairings of c and κ: $(c = c_{dg}, \kappa = \kappa_{dg})$, $(c = c_{sd}, \kappa = \kappa_{sd})$, $(c = c_{hu}, \kappa = \kappa_{hu})$, and $(c = c_+, \kappa = \kappa_+)$. Tables 5–10 contain the absolute errors, orders of accuracy, and maximum time-step limits for each of these schemes. Absolute errors (and by
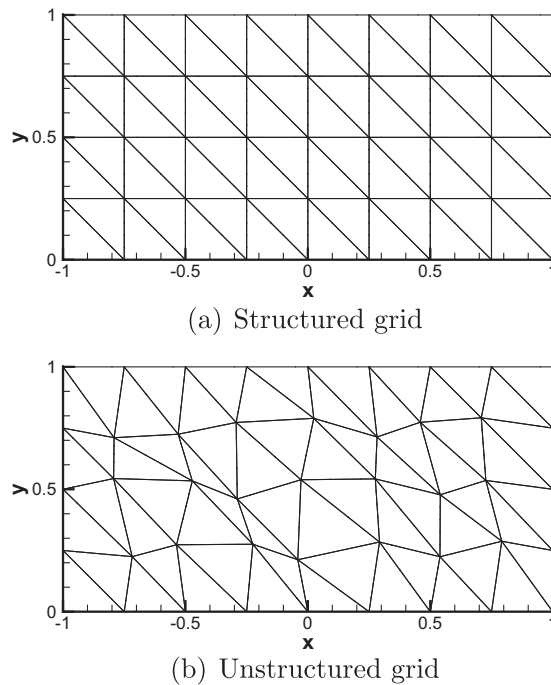
(a) Structured grid

(b) Unstructured grid

Fig. 4. Structured and unstructured triangular grids for the cases of $\tilde{N} = 4$ and $N = 64$.

extension orders of accuracy) were determined using L2 norms and seminorms of the errors in the total energy E and its gradient ∇E. The time-step limits (Δt_{max}) were determined using an iterative method on the structured grid with $\tilde{N} = 8$ and on the unstructured grid with $N = 256$.

Tables 5–8 demonstrate that the expected order of accuracy is obtained for all four schemes, for $p = 2$ and 3, on structured and unstructured grids. In addition, Tables 9 and 10 demonstrate that increasing c and κ increases the maximum time-step limit on structured and unstructured grids. In particular, for $p = 2$ on the structured grid with $\tilde{N} = 8$, the scheme with $c = c_+$ and $\kappa = \kappa_+$ has $\Delta t_{max} = 5.56\text{e-}03$, while the collocation-based nodal DG scheme (recovered with $c = 0$ and $\kappa = 0$) has $\Delta t_{max} = 3.19\text{e-}03$. Similarly, for $p = 2$ on the unstructured grid with $N = 256$, the scheme with $c = c_+$ and $\kappa = \kappa_+$ has $\Delta t_{max} = 4.96\text{e-}03$, while the collocation-based nodal DG scheme has $\Delta t_{max} = 2.88\text{e-}03$.

Overall, the time-step improvements originally observed for linear problems, for larger values of c and κ, have been shown to extend to nonlinear problems on structured and unstructured grids. Furthermore, these improvements appear to preserve accuracy (for the most part), as the expected order of accuracy was obtained for the vast majority of numerical experiments in this section.

6.2. Flow around SD7003 airfoil

In what follows, the VCJH schemes are employed to simulate the flow around an SD7003 airfoil. The SD7003 geometry is that of a low Reynolds number Selig/Donovan (SD) airfoil that has a maximum thickness of 9.2 percent at 30.9 percent chord, and a maximum camber of 1.2 percent at 38.3 percent chord [39]. Numerical experiments on the SD7003 geometry were performed on a circular domain with a radius of 50 chord-lengths, centered at the leading edge of the airfoil. Characteristic boundary conditions were prescribed on the outermost edge of the circular domain and adiabatic wall boundary conditions were prescribed on the surface of the airfoil. The computational domain was discretized into an unstructured grid with $N = 25,810$ triangular elements, as shown in Fig. 5. It should be noted, that, in order to facilitate the accurate representation of the SD7003 geometry, the edges of the triangular elements on the unstructured grid were defined in terms of 2nd order, quadratic polynomials.

At time $t = 0$, a uniform flow with the properties of air ($P_r = 0.72, \gamma = 1.4$) was initialized on the unstructured triangular grid. The incoming flow was given a Mach number of $M = 0.2$, a Reynolds number of 10,000, and an angle of entry of $4°$ (in order to simulate an angle of attack of $\alpha = 4°$). The solution was marched forward in time using the RK54 approach and, at each time-step, the inviscid and viscous numerical fluxes were computed using the Rusanov approach (with $\lambda = 1$) and the LDG approach (with $\beta = \pm 0.5\mathbf{n}_-$ and $\tau = 0.1$). Results from each simulation were evaluated after the lift and drag reached a pseudo-periodic state. Results were obtained on the unstructured grid with $N = 25,810$ for $p = 2$, for VCJH schemes with $c = c_{dg}$ and $\kappa = \kappa_{dg}$, and $c = c_+$ and $\kappa = \kappa_+$. Table 11 compares the time-averaged values of the lift and drag coefficients

Table 5
Accuracy of VCJH schemes for the Couette flow problem on structured triangular grids, for $p = 2$. The inviscid and viscous numerical fluxes were computed using a Rusanov flux with $\lambda = 1$ and a LDG flux with $\tau = 0.1$ and $\beta = \pm 0.5\mathbf{n}_-$.

c, κ	Grid	L_2 err.	$O(L_2)$	L_{2s} err.	$O(L_{2s})$
c_{dg}, κ_{dg}	$\bar{N} = 2$	3.02e−05		5.58e−04	
	$\bar{N} = 4$	3.19e−06	3.24	1.09e−04	2.36
	$\bar{N} = 8$	3.61e−07	3.14	2.37e−05	2.20
	$\bar{N} = 16$	4.37e−08	3.05	6.11e−06	1.95
c_{sd}, κ_{sd}	$\bar{N} = 2$	3.02e−05		4.94e−04	
	$\bar{N} = 4$	3.19e−06	3.24	9.93e−05	2.32
	$\bar{N} = 8$	3.61e−07	3.14	2.19e−05	2.18
	$\bar{N} = 16$	4.37e−08	3.05	5.61e−06	1.96
c_{hu}, κ_{hu}	$\bar{N} = 2$	3.02e−05		4.61e−04	
	$\bar{N} = 4$	3.19e−06	3.24	9.44e−05	2.29
	$\bar{N} = 8$	3.61e−07	3.14	2.10e−05	2.17
	$\bar{N} = 16$	4.37e−08	3.05	5.34e−06	1.98
c_+, κ_+	$\bar{N} = 2$	3.02e−05		4.20e−04	
	$\bar{N} = 4$	3.19e−06	3.24	8.90e−05	2.24
	$\bar{N} = 8$	3.61e−07	3.14	2.01e−05	2.15
	$\bar{N} = 16$	4.39e−08	3.04	5.04e−06	1.99

Table 6
Accuracy of VCJH schemes for the Couette flow problem on structured triangular grids, for $p = 3$. The inviscid and viscous numerical fluxes were computed using a Rusanov flux with $\lambda = 1$ and a LDG flux with $\tau = 0.1$ and $\beta = \pm 0.5\mathbf{n}_-$.

c, κ	Grid	L_2 err.	$O(L_2)$	L_{2s} err.	$O(L_{2s})$
c_{dg}, κ_{dg}	$\bar{N} = 2$	9.54e−07		2.80e−05	
	$\bar{N} = 4$	5.99e−08	3.99	3.93e−06	2.83
	$\bar{N} = 8$	3.78e−09	3.99	5.01e−07	2.97
	$\bar{N} = 16$	2.40e−10	3.97	6.11e−08	3.04
c_{sd}, κ_{sd}	$\bar{N} = 2$	9.53e−07		2.76e−05	
	$\bar{N} = 4$	5.98e−08	3.99	3.88e−06	2.83
	$\bar{N} = 8$	3.77e−09	3.99	4.96e−07	2.97
	$\bar{N} = 16$	2.39e−10	3.98	6.05e−08	3.04
c_{hu}, κ_{hu}	$\bar{N} = 2$	9.53e−07		2.77e−05	
	$\bar{N} = 4$	5.97e−08	4.00	3.89e−06	2.83
	$\bar{N} = 8$	3.76e−09	3.99	4.96e−07	2.97
	$\bar{N} = 16$	2.39e−10	3.98	6.05e−08	3.04
c_+, κ_+	$\bar{N} = 2$	9.52e−07		2.81e−05	
	$\bar{N} = 4$	5.97e−08	4.00	3.91e−06	2.84
	$\bar{N} = 8$	3.76e−09	3.99	4.99e−07	2.97
	$\bar{N} = 16$	2.38e−10	3.98	6.08e−08	3.04

for each of the schemes with the values obtained from the numerical experiments in [40]. In addition, Fig. 6 shows the density and vorticity contours obtained via the scheme with $c = c_+$ and $\kappa = \kappa_+$.

The data in Table 11 demonstrates that the results produced by the VCJH schemes are in close agreement with the results independently obtained by [40]. Overall, based on the tabulated data and the results in Fig. 6, it appears that the VCJH schemes are successful in simulating the temporal variation of lift and drag forces, and in accurately representing the rapidly evolving vortex structures that are formed in the shear layer that emanates from the trailing edge of the airfoil.

7. Conclusions

A FR formulation for solving advection–diffusion problems on triangular meshes has been presented. It has been proven that the formulation will be linearly stable for all orders of accuracy if the correction fields on triangles are chosen to be of VCJH type. Linear numerical experiments have demonstrated that certain schemes possess increased explicit time-step limits (compared with collocation-based nodal DG schemes of the same order), while maintaining the expected order of accu-

Table 7
Accuracy of VCJH schemes for the Couette flow problem on unstructured triangular grids, for $p = 2$. The inviscid and viscous numerical fluxes were computed using a Rusanov flux with $\lambda = 1$ and a LDG flux with $\tau = 0.1$ and $\beta = \pm 0.5\mathbf{n}_-$.

c, κ	Grid	L_2 err.	$O(L_2)$	L_{2s} err.	$O(L_{2s})$
c_{dg}, κ_{dg}	$N = 16$	6.32e−05		1.28e−03	
	$N = 64$	3.88e−06	4.03	1.38e−04	3.22
	$N = 256$	3.87e−07	3.33	2.54e−05	2.44
	$N = 1024$	4.51e−08	3.10	6.27e−06	2.02
c_{sd}, κ_{sd}	$N = 16$	6.31e−05		1.15e−03	
	$N = 64$	3.88e−06	4.03	1.27e−04	3.18
	$N = 256$	3.87e−07	3.33	2.36e−05	2.43
	$N = 1024$	4.50e−08	3.10	5.77e−06	2.03
c_{hu}, κ_{hu}	$N = 16$	6.31e−05		1.09e−03	
	$N = 64$	3.87e−06	4.03	1.22e−04	3.15
	$N = 256$	3.86e−07	3.32	2.27e−05	2.43
	$N = 1024$	4.50e−08	3.10	5.49e−06	2.05
c_+, κ_+	$N = 16$	6.30e−05		1.00e−03	
	$N = 64$	3.86e−06	4.03	1.16e−04	3.11
	$N = 256$	3.86e−07	3.32	2.17e−05	2.41
	$N = 1024$	4.52e−08	3.09	5.19e−06	2.07

Table 8
Accuracy of VCJH schemes for the Couette flow problem on unstructured triangular grids, for $p = 3$. The inviscid and viscous numerical fluxes were computed using a Rusanov flux with $\lambda = 1$ and a LDG flux with $\tau = 0.1$ and $\beta = \pm 0.5\mathbf{n}_-$.

c, κ	Grid	L_2 err.	$O(L_2)$	L_{2s} err.	$O(L_{2s})$
c_{dg}, κ_{dg}	$N = 16$	1.75e−06		4.91e−05	
	$N = 64$	7.77e−08	4.50	4.89e−06	3.33
	$N = 256$	4.22e−09	4.20	5.47e−07	3.16
	$N = 1024$	2.48e−10	4.09	6.27e−08	3.13
c_{sd}, κ_{sd}	$N = 16$	1.75e−06		4.69e−05	
	$N = 64$	7.76e−08	4.50	4.79e−06	3.29
	$N = 256$	4.20e−09	4.21	5.40e−07	3.15
	$N = 1024$	2.47e−10	4.09	6.21e−08	3.12
c_{hu}, κ_{hu}	$N = 16$	1.75e−06		4.66e−05	
	$N = 64$	7.75e−08	4.50	4.79e−06	3.28
	$N = 256$	4.20e−09	4.21	5.39e−07	3.15
	$N = 1024$	2.47e−10	4.09	6.21e−08	3.12
c_+, κ_+	$N = 16$	1.75e−06		4.65e−05	
	$N = 64$	7.74e−08	4.50	4.81e−06	3.27
	$N = 256$	4.19e−09	4.21	5.41e−07	3.15
	$N = 1024$	2.46e−10	4.09	6.24e−08	3.12

Table 9
Explicit time-step limits (Δt_{max}) of VCJH schemes on the structured triangular grid with $\bar{N} = 8$ for the Couette flow problem, for $p = 2$ and 3. The inviscid and viscous numerical fluxes were computed using a Rusanov flux with $\lambda = 1$ and a LDG flux with $\tau = 0.1$ and $\beta = \pm 0.5\mathbf{n}_-$.

	$p = 2$	$p = 3$
c_{dg}, κ_{dg}	3.19e−03	1.84e−03
c_{sd}, κ_{sd}	4.03e−03	2.29e−03
c_{hu}, κ_{hu}	4.58e−03	2.44e−03
c_+, κ_+	5.56e−03	2.67e−03

Table 10
Explicit time-step limits (Δt_{max}) of VCJH schemes on the unstructured triangular grid with $N = 256$ for the Couette flow problem, for $p = 2$ and 3. The inviscid and viscous numerical fluxes were computed using a Rusanov flux with $\lambda = 1$ and a LDG flux with $\tau = 0.1$ and $\beta = \pm 0.5\mathbf{n}_-$.

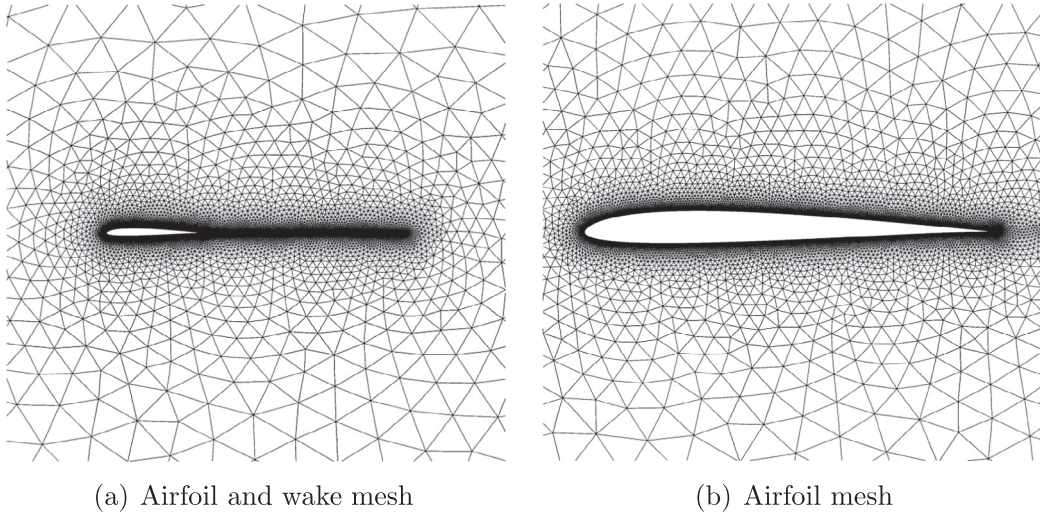|	$p = 2$	$p = 3$
c_{dg}, κ_{dg}	2.88e−03	1.57e−03
c_{sd}, κ_{sd}	3.62e−03	1.93e−03
c_{hu}, κ_{hu}	4.07e−03	2.06e−03
c_+, κ_+	4.96e−03	2.27e−03

(a) Airfoil and wake mesh   (b) Airfoil mesh

Fig. 5. Views of the unstructured triangular grid with $N = 25,810$ elements around the SD7003 airfoil geometry.

Table 11
Time-averaged values of the lift and drag coefficients for the SD7003 airfoil in air flow with $Re = 10,000$. The flow was simulated using the VCJH schemes with $p = 2$, $c = c_{dg}$, $\kappa = \kappa_{dg}$ and $c = c_+$, $\kappa = \kappa_+$ in conjunction with the Rusonav flux with $\lambda = 1$ and the LDG flux with $\beta = \pm 0.5\mathbf{n}_-$ and $\tau = 0.1$ on the unstructured triangular grid with $N = 25,810$ elements.

Source	$\overline{C_L}$	$\overline{C_D}$
Uranga et al. [40]	0.3755	0.04978
c_{dg}, κ_{dg}	0.3719	0.04940
c_+, κ_+	0.3713	0.04935

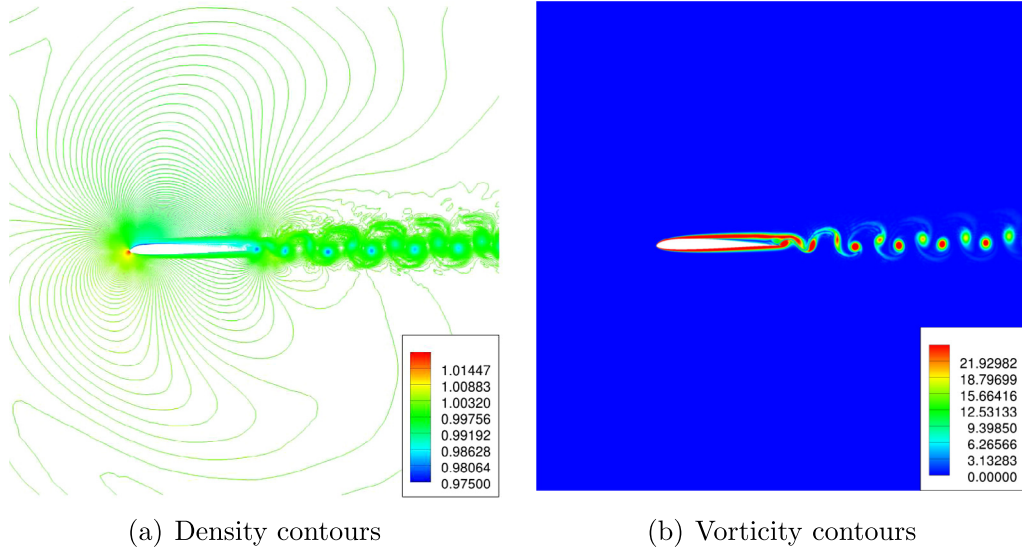
(a) Density contours   (b) Vorticity contours

Fig. 6. Density and vorticity contours for the flow with $Re = 10,000$ around the SD7003 airfoil. The flow was simulated using the VCJH scheme with $c = c_+$, $\kappa = \kappa_+$, and $p = 2$ in conjunction with the Rusonav flux with $\lambda = 1$ and the LDG flux with $\beta = \pm 0.5\mathbf{n}_-$ and $\tau = 0.1$ on the unstructured triangular grid with $N = 25,810$ elements.

racy. Furthermore, nonlinear numerical experiments (involving the Navier–Stokes equations) have demonstrated that the favorable performance of these schemes will likely extend to real-world problems.

Appendix A. VCJH correction fields and their role as lifting operators

Consider the vector correction function $\mathbf{g}_{f,j}$ and scalar correction field ('lifting operator') $\psi_{f,j}$, where $\psi_{f,j} = \hat{\nabla} \cdot \mathbf{g}_{f,j}$. The correction field $\psi_{f,j}$ can be classified as a 'VCJH correction field' if it takes the following form

$$\psi_{f,j} = \sum_{k=1}^{N_p} v_k L_k(\mathbf{r}), \tag{A.1}$$

where each $L_k(\mathbf{r})$ is an orthonormal polynomial of degree $\leqslant p$ (defined on $\mathbf{\Omega}_S$), and each coefficient v_k is obtained from the following system of equations

$$\sum_{k=1}^{N_p} v_k \sum_{m=1}^{p+1} \kappa_m \left(D^{(m,p)} L_i \right) \left(D^{(m,p)} L_k \right) = -v_i + \int_{\Gamma_S} (\mathbf{g}_{f,j} \cdot \hat{\mathbf{n}}) L_i d\Gamma_s \qquad \text{for } 1 \leqslant i \leqslant N_p, \tag{A.2}$$

where each $D^{(m,p)}$ is a derivative operator of degree p (defined by Eq. (41) in Section 3).

In Eq. (A.2), each constant κ_m is defined as

$$\kappa_m = \kappa \binom{p}{m-1} = \kappa \left[\frac{p!}{(m-1)!(p-m+1)!} \right], \quad 0 \leqslant \kappa \leqslant \infty, \tag{A.3}$$

and hence the correction fields $\psi_{f,j}$ are parameterized by the scalar κ.

As currently constructed, the correction fields $\psi_{f,j}$ possess an important ability to act as 'lifting operators', which transform $\hat{u}^C$ defined on the element boundary Γ_S into $\hat{\nabla}\hat{u}^C$ defined within the element interior $\mathbf{\Omega}_S$, according to the following identity

$$\int_{\mathbf{\Omega}_S} \hat{\nabla}\hat{u}^C d\mathbf{\Omega}_S = \int_{\Gamma_S} \hat{u}^C \hat{\mathbf{n}} d\Gamma_S. \tag{A.4}$$

In what follows, the derivation of this identity will be examined.

First, recall that $\psi_{f,j} = \hat{\nabla} \cdot \mathbf{g}_{f,j}$, and thus according to the divergence theorem, $\mathbf{g}_{f,j}$ and $\psi_{f,j}$ are related as follows

$$\int_{\mathbf{\Omega}_S} \psi_{f,j} d\mathbf{\Omega}_S = \int_{\Gamma_S} \mathbf{g}_{f,j} \cdot \hat{\mathbf{n}} d\Gamma_S. \tag{A.5}$$

The quantity $\mathbf{g}_{f,j} \cdot \hat{\mathbf{n}}$ (which satisfies Eq. (34) with $\mathbf{g}_{f,j}$ in place of $\mathbf{h}_{f,j}$) vanishes on all faces except for face f. As a result, Eq. (A.5) becomes

$$\int_{\mathbf{\Omega}_S} \psi_{f,j} d\mathbf{\Omega}_S = \int_{\Gamma_f} \mathbf{g}_{f,j} \cdot \hat{\mathbf{n}}_{f,j} d\Gamma_f. \tag{A.6}$$

Multiplying Eq. (A.6) by $\hat{u}^C_{f,j}$ and $\hat{\mathbf{n}}_{f,j}$, and summing over f and j yields

$$\int_{\mathbf{\Omega}_S} \sum_{f=1}^{3} \sum_{j=1}^{N_{fp}} \hat{u}^C_{f,j} \psi_{f,j} \hat{\mathbf{n}}_{f,j} d\mathbf{\Omega}_S = \sum_{f=1}^{3} \left[\int_{\Gamma_f} \sum_{j=1}^{N_{fp}} \hat{u}^C_{f,j} (\mathbf{g}_{f,j} \cdot \hat{\mathbf{n}}_{f,j}) \hat{\mathbf{n}}_{f,j} d\Gamma_f \right]. \tag{A.7}$$

Substituting Eq. (24) into this equation, and replacing the term $\mathbf{g}_{f,j} \cdot \hat{\mathbf{n}}_{f,j}$ with the 1D Lagrange polynomial $\hat{l}^{1D}_{f,j}$ (because $\mathbf{g}_{f,j} \cdot \hat{\mathbf{n}}_{f,j}$ satisfies Eq. (34) and $\mathbf{g}_{f,j} \in RT_p(\mathbf{\Omega}_S)$), one obtains

$$\int_{\mathbf{\Omega}_S} \hat{\nabla}\hat{u}^C d\mathbf{\Omega}_S = \sum_{f=1}^{3} \left[\int_{\Gamma_f} \sum_{j=1}^{N_{fp}} \hat{u}^C_{f,j} \hat{l}^{1D}_{f,j} \hat{\mathbf{n}}_{f,j} d\Gamma_f \right]. \tag{A.8}$$

Note that the 1D Lagrange polynomial $\hat{l}^{1D}_{f,j}$ is a degree p polynomial on face f, which takes on the value of 1 at flux point j, and the value of 0 at all other flux points on the face.

A corollary to the divergence theorem requires that

$$\int_{\mathbf{\Omega}_S} \hat{\nabla}\hat{u}^C d\mathbf{\Omega}_S = \int_{\Gamma_S} \hat{u}^C \hat{\mathbf{n}} d\Gamma_S = \sum_{f=1}^{3} \left[\int_{\Gamma_f} \hat{u}^C |_{\Gamma_f} \hat{\mathbf{n}}_f d\Gamma_f \right]. \tag{A.9}$$

From Eqs. (A.8) and (A.9), one obtains

$$\sum_{f=1}^{3} \left[\int_{\Gamma_f} \hat{u}^C |_{\Gamma_f} \hat{\mathbf{n}}_f d\Gamma_f \right] = \sum_{f=1}^{3} \left[\int_{\Gamma_f} \sum_{j=1}^{N_{fp}} \hat{u}^C_{f,j} \hat{l}^{1D}_{f,j} \hat{\mathbf{n}}_{f,j} d\Gamma_f \right]. \tag{A.10}$$

Each domain Γ_f is arbitrary (as the standard element and its associated faces can be chosen arbitrarily) and thus the integrands in Eq. (A.10) must be equal. Consequently, $\hat{u}^C$ on Γ_S takes the form

$$\hat{u}^C|_{\Gamma_f} = \sum_{j=1}^{N_{fp}} \hat{u}^C_{f,j} \hat{l}^{1D}_{f,j} \quad \hat{u}^C|_{\Gamma_S} = \begin{cases} \hat{u}^C|_{\Gamma_1} & \text{on } \boldsymbol{\Gamma}_1 \\ \hat{u}^C|_{\Gamma_2} & \text{on } \boldsymbol{\Gamma}_2 \\ \hat{u}^C|_{\Gamma_3} & \text{on } \boldsymbol{\Gamma}_3 \end{cases}. \tag{A.11}$$

In conclusion, the VCJH correction fields $\psi_{f,j}$ serve as 'lifting operators', because they provide a relationship (given by Eq. (A.9)) between $\hat{u}^C$ defined on $\boldsymbol{\Gamma}_S$ (Eq. (A.11)) and $\hat{\nabla}\hat{u}^C$ defined within $\boldsymbol{\Omega}_S$ (Eq. (24)).

Appendix B. Supplemental derivations for the stability proof

In what follows, Eqs. (68) and (69) for Lemma 4.3 are derived.
Upon performing integration by parts on Eq. (66) and rearranging the result, one obtains

$$\int_{\Gamma_S} (\mathbf{h}_{f,j} \cdot \hat{\mathbf{n}}) L_i \, d\Gamma_S = \int_{\Omega_S} \phi_{f,j} L_i \, d\Omega_S + \sum_{m=1}^{p+1} c_m \left(D^{(m,p)} L_i\right) \left(D^{(m,p)} \phi_{f,j}\right). \tag{B.1}$$

Note that $\hat{u}^D \in P_p(\boldsymbol{\Omega}_S)$ can be written as a linear combination of the orthonormal polynomials L_i. As a result, Eq. (B.1) can be rewritten in terms of $\hat{u}^D$ as follows

$$\int_{\Gamma_S} (\mathbf{h}_{f,j} \cdot \hat{\mathbf{n}}) \hat{u}^D \, d\Gamma_S = \int_{\Omega_S} \phi_{f,j} \hat{u}^D \, d\Omega_S + \sum_{m=1}^{p+1} c_m \left(D^{(m,p)} \hat{u}^D\right) \left(D^{(m,p)} \phi_{f,j}\right). \tag{B.2}$$

On multiplying Eq. (B.2) by $\Delta_{f,j}$ and summing over f and j, one obtains

$$\int_{\Gamma_S} \left(\sum_{f=1}^{3} \sum_{j=1}^{N_{fp}} \Delta_{f,j} \mathbf{h}_{f,j} \cdot \hat{\mathbf{n}}\right) \hat{u}^D \, d\Gamma_S = \int_{\Omega_S} \left(\sum_{f=1}^{3} \sum_{j=1}^{N_{fp}} \Delta_{f,j} \phi_{f,j}\right) \hat{u}^D \, d\Omega_S + \sum_{m=1}^{p+1} c_m \left(D^{(m,p)} \hat{u}^D\right) \left(D^{(m,p)} \left(\sum_{f=1}^{3} \sum_{j=1}^{N_{fp}} \Delta_{f,j} \phi_{f,j}\right)\right). \tag{B.3}$$

Upon substituting the definition of $\hat{\mathbf{f}}^C$ (Eq. (35)) into Eq. (B.3) and rearranging the result, one obtains Eq. (68).
Eq. (69) can be obtained as follows. Consider performing integration by parts on Eq. (67) and rearranging the result, in order to obtain

$$\int_{\Gamma_S} (\mathbf{g}_{f,j} \cdot \hat{\mathbf{n}}) L_i \, d\Gamma_S = \int_{\Omega_S} \psi_{f,j} L_i \, d\Omega_S + \sum_{m=1}^{p+1} \kappa_m \left(D^{(m,p)} L_i\right) \left(D^{(m,p)} \psi_{f,j}\right). \tag{B.4}$$

On the LHS, $\mathbf{g}_{f,j} \cdot \hat{\mathbf{n}}$ vanishes on all faces except for face f (as required by Eq. (34)). As a result, Eq. (B.4) becomes

$$\int_{\Gamma_f} (\mathbf{g}_{f,j} \cdot \hat{\mathbf{n}}_{f,j}) L_i \, d\Gamma_f = \int_{\Omega_S} \psi_{f,j} L_i \, d\Omega_S + \sum_{m=1}^{p+1} \kappa_m \left(D^{(m,p)} L_i\right) \left(D^{(m,p)} \psi_{f,j}\right). \tag{B.5}$$

Because $(\hat{\mathbf{f}}^D_{dif} \cdot \hat{\mathbf{n}}_{f,j}) \in P_p(\boldsymbol{\Omega}_S)$, it can be expressed as a linear combination of the orthonormal polynomials L_i and therefore, Eq. (B.5) can be rewritten with $(\hat{\mathbf{f}}^D_{dif} \cdot \hat{\mathbf{n}}_{f,j})$ in place of L_i as follows

$$\int_{\Gamma_f} (\mathbf{g}_{f,j} \cdot \hat{\mathbf{n}}_{f,j}) \left(\hat{\mathbf{f}}^D_{dif} \cdot \hat{\mathbf{n}}_{f,j}\right) d\Gamma_f = \int_{\Omega_S} \psi_{f,j} \left(\hat{\mathbf{f}}^D_{dif} \cdot \hat{\mathbf{n}}_{f,j}\right) d\Omega_S + \sum_{m=1}^{p+1} \kappa_m \left(D^{(m,p)} \left(\hat{\mathbf{f}}^D_{dif} \cdot \hat{\mathbf{n}}_{f,j}\right)\right) \left(D^{(m,p)} \psi_{f,j}\right). \tag{B.6}$$

On multiplying Eq. (B.6) by $\hat{u}^C_{f,j}$ and summing over f and j, one obtains

$$\sum_{f=1}^{3} \left[\int_{\Gamma_f} \sum_{j=1}^{N_{fp}} \hat{u}^C_{f,j} (\mathbf{g}_{f,j} \cdot \hat{\mathbf{n}}_{f,j}) \left(\hat{\mathbf{f}}^D_{dif} \cdot \hat{\mathbf{n}}_{f,j}\right) d\Gamma_f \right] = \int_{\Omega_S} \hat{\mathbf{f}}^D_{dif} \cdot \left(\sum_{f=1}^{3} \sum_{j=1}^{N_{fp}} \hat{u}^C_{f,j} \psi_{f,j} \hat{\mathbf{n}}_{f,j}\right) d\Omega_S + \sum_{m=1}^{p+1} \kappa_m D^{(m,p)} (\hat{\mathbf{f}}^D_{dif})$$

$$\cdot D^{(m,p)} \left(\sum_{f=1}^{3} \sum_{j=1}^{N_{fp}} \hat{u}^C_{f,j} \psi_{f,j} \hat{\mathbf{n}}_{f,j}\right). \tag{B.7}$$

Upon combining Eqs. (24), (A.11), and (B.7) and rearranging the result, one obtains Eq. (69).

References

[1] B. Cockburn, S. Hou, C. Shu, The Runge–Kutta local projection discontinuous Galerkin finite element method for conservation laws IV: the multidimensional case, Math. Comput. 54 (1990) 545–581.
[2] F. Bassi, S. Rebay, High-order accurate discontinuous finite element solution of the 2D Euler equations, J. Comput. Phys. 138 (1997) 251–285.
[3] F. Bassi, S. Rebay, A high-order accurate discontinuous finite element method for the numerical solution of the compressible Navier-Stokes equations, J. Comput. Phys. 131 (1997) 267–279.
[4] D.A. Kopriva, J.H. Kolias, A conservative staggered-grid Chebyshev multidomain method for compressible flows, J. Comput. Phys. 125 (1996) 244–261.
[5] Y. Liu, M. Vinokur, Z.J. Wang, Spectral difference method for unstructured grids I: basic formulation, J. Comput. Phys. 216 (2006) 780–801.
[6] H. Huynh, A flux reconstruction approach to high-order schemes including discontinuous Galerkin methods, AIAA P., in: 18th AIAA Computational Fluid Dynamics Conference, Miami, FL, Jun 25–28, 2007.

[7] H. Huynh, A reconstruction approach to high-order schemes including discontinuous Galerkin for diffusion, AIAA P., in: 47th AIAA Aerospace Sciences Meeting, Orlando, FL, Jan 5–8, 2009.
[8] H. Huynh, High-order methods including discontinuous Galerkin by reconstructions on triangular meshes, AIAA P., in: 49th AIAA Aerospace Sciences Meeting, Orlando, FL, Jan 4–7, 2011.
[9] H. Gao, Z.J. Wang, A high-order lifting collocation penalty formulation for the Navier–Stokes equations on 2D mixed grids, AIAA P., in: 19th AIAA Computational Fluid Dynamics Conference, San Antonio, TX, June 22–25, 2009.
[10] Z. Wang, H. Gao, A unifying lifting collocation penalty formulation including the discontinuous Galerkin, spectral volume/difference methods for conservation laws on mixed grids, J. Comput. Phys. 228 (2009) 8161–8186.
[11] M. Yu, Z. Wang, On the connection between the correction and weighting functions in the correction procedure via reconstruction method, J. Scient. Comput. (2012). DOI: 10.1007/s10915-012-9618-3.
[12] T. Haga, H. Gao, Z. Wang, A high-order unifying discontinuous formulation for the Navier-Stokes equations on 3D mixed grids, Math. Model. Nat. Phenom. 6 (2011) 28–56.
[13] T. Haga, H. Gao, Z. Wang, A high-order unifying discontinuous formulation for 3D mixed grids, AIAA P., in: 48th AIAA Aerospace Sciences Meeting, Orlando, FL, Jan 4–7, 2010.
[14] J. Nordström, K. Forsberg, C. Adamsson, P. Eliasson, Finite volume methods, unstructured meshes and strict stability for hyperbolic problems, Appl. Numer. Math. 45 (2003) 453–473.
[15] F. Ham, Improved scalar transport for unstructured finite volume methods using simplex superposition, Annual Research Briefs, Center for Turbulence Research, NASA-AMES (2008) 347–358.
[16] H. Kreiss, G. Scherer, Finite element and finite difference methods for hyperbolic partial differential equations, Math. Aspect. Finite Elem. Part. Differ. Equat. (1974) 195–212. Publ. Math. Res. Center Univ. Wisconsi.
[17] H. Kreiss, G. Scherer, On the existence of energy estimates for difference approximations for hyperbolic systems, Tech. Rep., Uppsala University, Division of Scientific Computing, 1977.
[18] M. Carpenter, D. Gottlieb, S. Abarbanel, Time-stable boundary conditions for finite-difference schemes solving hyperbolic systems: methodology and application to high-order compact schemes, J. Comput. Phys. 111 (1994) 220–236.
[19] M. Carpenter, J. Nordström, D. Gottlieb, A stable and conservative interface treatment of arbitrary spatial accuracy, J. Comput. Phys. 148 (1999) 341–365.
[20] A. Jameson, A proof of the stability of the spectral difference method for all orders of accuracy, J. Scient. Comput. 45 (2010) 348–358.
[21] P.E. Vincent, P. Castonguay, A. Jameson, A new class of high-order energy stable flux reconstruction schemes, J. Scient. Comput. 47 (2011) 50–72.
[22] D.M. Williams, P. Castonguay, P.E. Vincent, A. Jameson, An extension of energy stable flux reconstruction to unsteady, non-linear, viscous problems on mixed grids, AIAA P., in: 20th AIAA Computational Fluid Dynamics Conference, Honolulu, Hawaii, June 27–30, 2011.
[23] P. Castonguay, High-Order Energy Stable Flux Reconstruction Schemes for Fluid Flow Simulations on Unstructured Grids, Ph.D. thesis, Stanford University, 2012.
[24] P. Castonguay, D.M. Williams, P.E. Vincent, A. Jameson, Energy stable flux reconstruction for advection-diffusion problems, Comput. Meth. Appl. Mech. Eng., 2012.
[25] P. Castonguay, P.E. Vincent, A. Jameson, A new class of high-order energy stable flux reconstruction schemes for conservation laws on triangular grids, J. Scient. Comput. (2011). http://dx.doi.org/10.1007/s10915-012-9618-3.
[26] H. Viviand, Conservative forms of gas dynamic equations, La Recherche Aerospatiale 1 (1974) 65–66.
[27] M. Vinokur, Conservation equations of gasdynamics in curvilinear coordinate systems, J. Comput. Phys. 14 (1974) 105–125.
[28] J. Hesthaven, T. Warburton, Nodal Discontinuous Galerkin methods: Algorithms, Analysis, and Applications, Springer Verlag, 2007.
[29] B. Cockburn, C. Shu, The local discontinuous Galerkin method for time-dependent convection-diffusion systems, SIAM J. Numer. Anal. 35 (1998) 2440–2463.
[30] J. Peraire, P. Persson, The compact discontinuous Galerkin (CDG) method for elliptic problems, SIAM J. Scient. Comput. 30 (2009) 1806–1824.
[31] D. Arnold, An interior penalty finite element method with discontinuous elements, SIAM J. Numer. Anal. 19 (1982) 742–760.
[32] F. Bassi, S. Rebay, G. Mariotti, S. Pedinotti, M. Savini, A high-order accurate discontinuous finite element method for inviscid and viscous turbomachinery flows, in: R. Decuypere, G. Dibelius (Eds.), 2nd European Conference on Turbomachinery Fluid Dynamics and Thermodynamics (Antwerpen, Belgium), Technologisch Instituut, 1997, pp. 99–108.
[33] P.L. Roe, Approximate riemann solvers, parameter vectors and difference schemes, J. Comput. Phys. 43 (1981) 357–372.
[34] V.V. Rusanov, Calculation of interaction of non-steady shock waves with obstacles, J. Comput. Math. Phys. USSR 1 (1961) 261–279.
[35] P. Raviart, J. Thomas, A mixed finite element method for second-order elliptic problems, Math. Aspect. Finite Elem. Meth. (1977) 292–315.
[36] M. Dubiner, Spectral methods on triangles and other domains, J. Scient. Comput. 6 (1991) 345–390.
[37] M.H. Carpenter, C. Kennedy, Fourth-order 2N-storage Runge–Kutta schemes, Technical Report TM 109112, NASA, NASA Langley Research Center, 1994.
[38] P. Castonguay, P.E. Vincent, A. Jameson, Application of energy stable flux reconstruction schemes for the Euler equations, AIAA P., in: 49th AIAA Aerospace Sciences Meeting, Orlando, FL, Jan 4–7, 2011.
[39] UIUC Applied Aerodynamics Group. UIUC airfoil coordinates database, http://www.ae.illinois.edu/m-selig/ads/coord_database.html, Retrieved April 2013.
[40] A. Uranga, P.-O. Persson, M. Drela, J. Peraire, Implicit large eddy simulation of transition to turbulence at low Reynolds numbers using a discontinuous Galerkin method, Int. J. Numer. Meth. Eng., 87 (1–5) (2011) 232–261.